Article

In Vivo Formation of HgSe Nanoparticles and Hg–Tetraselenolate Complex from Methylmercury in Seabirds—Implications for the Hg–Se Antagonism

Alain Manceau,* Anne-Claire Gaillot, Pieter Glatzel, Yves Cherel, and Paco Bustamante

Read Online

ACCESS | Metrics & More | Article Recommendations | Supporting Information

ABSTRACT: In vivo and in vitro evidence for detoxification of methylmercury (MeHg) as insoluble mercury selenide (HgSe) underlies the central paradigm that mercury exposure is not or little hazardous when tissue Se is in molar excess (Se:Hg > 1). However, this hypothesis overlooks the binding of Hg to selenoproteins, which lowers the amount of bioavailable Se that acts as a detoxification reservoir for MeHg, thereby underestimating the toxicity of mercury. This question was addressed by determining the chemical forms of Hg in various tissues of giant petrels *Macronectes* spp. using a combination of high energy-resolution X-ray absorption near edge structure and extended X-ray absorption fine structure spectroscopy, and transmission electron microscopy coupled to elemental mapping. Three main Hg species were identified, a MeHg-cysteinate complex, a four-coordinate selenocysteinate complex ($Hg(Sec)_4$), and a HgSe precipitate, together with a minor dicysteinate complex $Hg(Cys)_2$. The amount of HgSe decreases in the order liver > kidneys > brain = muscle, and the amount of $Hg(Sec)_4$ in the order muscle > kidneys > brain > liver. On the basis of biochemical considerations and structural modeling, we hypothesize that $Hg(Sec)_4$ is bound to the carboxy-terminus domain of selenoprotein P (SelP) which contains 12 Sec residues. Structural flexibility allows SelP to form multinuclear $Hg_x(Se,Sec)_y$ complexes, which can be biomineralized to HgSe by protein self-assembly. Because $Hg(Sec)_4$ has a Se:Hg molar ratio of 4:1, this species severely depletes the stock of bioavailable Se for selenoprotein synthesis and activity to one μg Se/g dry wet in the muscle of several birds. This concentration is still relatively high because selenium is naturally abundant in seawater, therefore it probably does not fall below the metabolic need for essential selenium. However, this study shows that this may not be the case for terrestrial animals, and that muscle may be the first tissue potentially injured by Hg toxicity.

KEYWORDS: *Mercury, bird, speciation, selenoprotein P, selenocysteine, HR-XANES, EXAFS, STEM-HAADF, STEM-EDX*
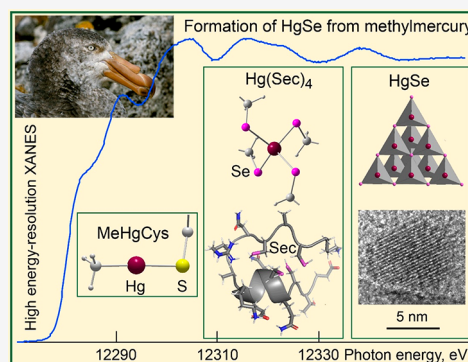
INTRODUCTION

Being top predators in aquatic food webs, large seabirds are particularly exposed to methylmercury (MeHg). The total mercury concentration commonly reaches several hundreds of μg/g dry weight (dw) in liver of old individuals, several tens μg/g dw in feathers, muscle, and kidneys, and several μg/g dw in blood of piscivorous and scavenger seabirds from the southern ocean.[1−8] Mercury concentrations are positively correlated with selenium concentrations in the liver.[9−14] Because mercury has a higher affinity for selenium than for sulfur,[15] the Hg−Se correlation is attributed chemically to the binding of Hg(II) to Se(-II). The Hg−Se antagonism is well documented experimentally[16−18] and in wildlife.[19−21] Mercury selenide (HgSe) is the most common inorganic selenious form in biological tissues. HgSe particles occur predominantly in the liver, and in lesser amounts in the muscle, kidneys, brain, lung, pancreas, and spleen of aquatic mammals (pinnipeds and cetaceans).[22−26] Mercury sulfide (β-HgS), as an admixture of primary HgSe, has been observed in the liver of the beluga whale *Delphinapterus leucas*.[27] Selenium and sulfur can also occur in solid solution $Hg(S_x,Se_y)$, as in the liver of the black-footed albatross (*Phoebastria nigripes*).[22] According to the best of the authors' knowledge, no other Hg form is known in seabirds.

The Hg−C bond of MeHg is cleaved readily by selenoamino acids under physiologically relevant experimental conditions yielding HgSe as the end product.[28] Hence, the biomineralization of potentially inert and apparently nontoxic HgSe granules observed in wildlife is considered as the main detoxification mechanism of MeHg. Consequently, the capacity for an organism to detoxify MeHg depends on the Hg:Se molar ratio, which represents the fraction of Se bound to Hg.[29−34]
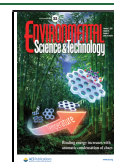
Methylmercury is more hazardous when the Hg level approaches or exceeds equimolar stoichiometry with Se (i.e., Hg:Se ≥ 1),[35,36] to the point of inducing a conditioned deficiency of bioavailable Se for selenoenzyme synthesis and activity.[37,38] Therefore, the difference of molar content between Se and Hg ($[Se]_{mol} − [Hg]_{mol}$) is considered to reflect mercury sequestration and selenium depletion, and is widely used to assess Hg exposure risk.[12,36,39−41] Gajdosechova and co-workers[26] cautioned that this approach may be deceptive, however, because the cells may contain other selenious forms of Hg than HgSe with a Hg:Se ratio different from one.

In addition to selenoamino acids, demethylation reactions can be mediated also by low molecular weight seleniol molecules, such as selenoneine,[42] and selenoproteins, such as selenoprotein P (SelP).[43] Selenoneine has been identified in fish,[44] in cetacean and in red blood cells of Inuits,[45] and Hg-bound SelP has been identified in the plasma of Inuits[46] and miners exposed to mercury[47] and in the liver, kidneys, and muscle of the waterbird Clark's grebe (*Aechmophorus clarkii*).[43] The demethylated mercury atoms are coordinated to four selenocysteine residues (Hg(Sec)$_4$ complex) in SelP.[43] The coordination number of Hg with selenoneine is unknown, however, it is probably also four because this coordination is easy to obtain at Se:Hg = 4 with synthetic derivatives analogue to selenoneine,[48] whereas it requires a high excess of sulfur with thiolate ligands.[49,50] This difference is explained, on the one hand by the greater selenophilicity than thiophilicity of Hg,[15] and on the other hand by the better nucleophilicity and higher acidity of the selenolate anion ($pK_a(−SeH) = 5.4$) than the thiolate anion ($pK_a(−SH) = 8.2$).[51] Thus, tetrahedral bonding with four selenium atoms appears to be the preferred coordination of Hg in organic molecules. The tetraselenolate complex having a Hg:Se molar ratio of 1:4 compared to 1:1 for HgSe, all the Hg can be bound to Se at a Hg:Se ratio much lower than 1:1. Therefore, overlooking the Hg(Sec)$_4$ species leads to an overestimate of the amount of bioavailable Se and in turn to underestimate the toxicity of mercury.

Here, we report the chemical forms of mercury in the feathers, blood, liver, kidneys, muscle, and brain of giant petrels (*Macronectes* spp.), as determined using Hg L$_3$-edge high energy-resolution X-ray absorption near edge structure (HR-XANES)[43,52−62] and extended X-ray absorption fine structure (EXAFS) spectroscopy,[63] high resolution transmission electron microscopy (HRTEM), and high-angle annular dark-field scanning transmission electron microscopy (STEM-HAADF) coupled to elemental mapping from energy dispersive X-ray spectrometry (EDX). Coupled with chemical analyses, the quantitative speciation data allowed calculating the concentration of bioavailable Se ($[Se]_{bio}$), the molar fraction of bioavailable Se to total Se ($[Se]_{bio}:[Se]_{tot}$), and the *effective* (or biological) fraction of Se bound to Hg ($(Hg:Se)_{eff}$), and to discuss the toxicity of mercury from a speciation perspective.

■ MATERIALS AND METHODS

A detailed description of the bird samples, experimental methods, and data analysis is given in the Supporting Information (SI).

Samples. Eight dead giant petrels were opportunistically collected in French Southern and Antarctic Lands (Table S1). Individuals were stored at −20 °C until dissection and the tissues lyophilized for chemical analysis and spectroscopic measurement. Freeze-drying a frozen tissue does not change

the speciation of the metal.[56,64] Age and breeding status of the birds are not known but all are adult males. Because females can eliminate part of their Hg load trough egg production, we selected males to avoid the effect of maternal transfer on Hg metabolism. We studied the Hg speciation in the feathers, liver, kidneys, and muscle from five petrels (P1−P5), in the blood from three out of the five (P1−P3), and in the brain from three other birds (P6−P8) (Table S2). The 26 tissues were analyzed by HR-XANES, and two liver, two kidney, and three muscle tissues by EXAFS.

Hg and Se Analyses. Total mercury was quantified with an AMA-254 mercury analyzer (Altec, Prague; limit of detection, LOD, 0.005 μg/g dw; aliquot mass: 0.5−5 mg dw) and total selenium with a Thermo Fisher Scientific X Series 2 ICP−MS (LOD 0.08 μg/g dw; aliquots mass: 20−300 mg dw).

HR-XANES and EXAFS Spectroscopy. Mercury L$_3$-edge HR-XANES and EXAFS spectra were measured at 10−15 K with high-reflectivity analyzer crystals[65] on beamline ID26 at the European Synchrotron Radiation Facility (ESRF). HR-XANES data were analyzed by principal component analysis (PCA[66]) and target transformation[67,68] against a large database of spectra described previously.[43,52,54−56,59] All reference spectra were considered as a basis for identification of the Hg species, but only diagnostic spectra are discussed herein. The molar proportions (mol %) of the Hg species in the petrel tissues were obtained by linear combination fitting analysis. The accuracy of the amount of a fitted component was estimated to be equal to the variation of its value when the fit residual (NSS) was increased by 20%. NSS is the normalized sum-squared difference between two spectra expressed as $\Sigma[(y_{exp} − y_{fit})^2]/\Sigma(y_{exp}^2)$.

Electron Microscopy. Scanning transmission electron microscopy (STEM) images were acquired on Nant'Themis, a Themis Z G3 Cs-probe corrected microscope (Thermo Fisher Scientific) operated at 80 kV (or 300 kV in cryo mode) and equipped with a high-angle annular dark field (HAADF) detector (resolution ~1.0 Å and 80 kV). Elemental maps were acquired in STEM mode using a Super-X emission X-ray spectrometer consisting of four windowless silicon-drift detectors (SDDs) providing a large collection solid angle of 0.7 srad. Additional high-resolution TEM (HRTEM) images and selected-area electron diffraction (SAED) patterns were acquired at 300 kV on a GATAN OneView camera (resolution ~1.8 Å). The liver, kidney, and muscle tissues of individual P4 (Tables S1 and S2) were dispersed in ethanol and deposited on a lacey-C copper grid.

■ RESULTS

Mercury and Selenium Concentrations. The amounts of Hg and Se are extremely variable between and within birds. The dry weight concentrations of Hg range from 170 to 1499 μg/g in liver (n = 7), from 9.8 to 414 μg/g in kidneys (n = 8), from 2.9 to 88.7 μg/g in muscle (n = 8), from 4.8 to 26.2 μg/g in feathers (n = 8), from 1.3 to 23.9 μg/g in blood (n = 8), and from 1.6 to 13.2 μg/g in brain (n = 3) (Table S2). The majority of the Hg concentrations are close to, and sometimes above, the highest values reported to date in seabird tissues,[6−8,69,70] but remain below values reported for marine mammals.[71,72] The corresponding ranges of Se concentrations are 109−1101 μg/g dw in liver (n = 7), 55−363 μg/g in kidneys (n = 8), 10.1−72.7 μg/g in muscle (n = 8), 5.9−24.2 μg/g in feathers (n = 8), 43.4−118 μg/g in blood (n = 8), and

26.2−47.0 μg/g in brain ($n = 3$). The liver always contains the highest levels of Hg and Se, as a result of its detoxification role and the toxicological Hg−Se antagonism.[19] The concentrations of Hg and Se in nonhepatic tissues relative to their concentrations in liver decrease in the following order: for Hg, liver (100%) > kidneys (14.5 ± 8.6%) > muscle (5.9 ± 3.5%) > feathers (3.8 ± 1.9%) > brain (2.3 ± 1.4%) > blood (1.9 ± 2.0%), and for Se, liver (100%) > kidneys (65.5 ± 39.5%) > blood (42.6 ± 31.2%) > brain (31.3 ± 9.5%) > muscle (15.3 ± 8.4%) > feathers (6.1 ± 7.0%) (Figure 1). The blood selenium
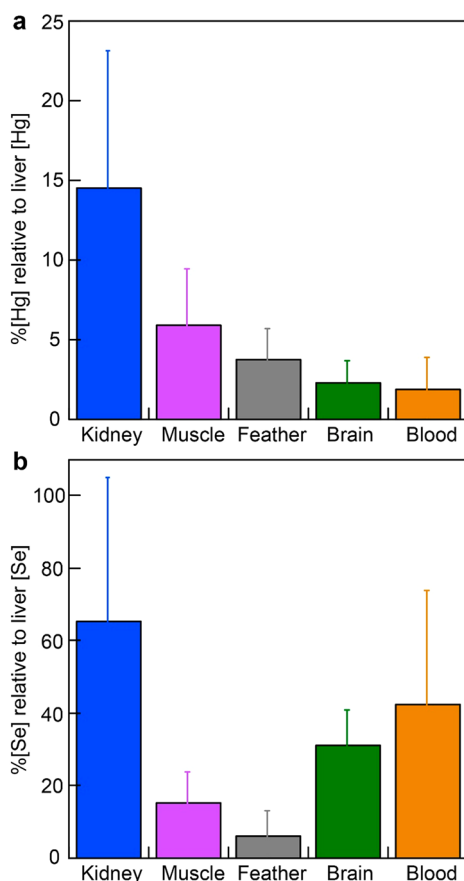

Figure 1. Bar charts of the Hg (a) and Se (b) levels in giant petrel tissues, as expressed as a percentage of the liver levels.

level is particularly high, between 0.5 and 1.2 μmol/g, which is 30 to 90 times more than Hg on a molar basis. The high blood selenium is explained by the Se-rich diet and by the metabolic function of the liver, which sequesters Hg and secretes SelP into the plasma to supply Se to endocrine tissues to synthesize selenoproteins they need for their metabolism.[38,33,38,73−76]

The relationship between the molar concentrations of Se and Hg in petrel tissues is shown in Figure 2a. The Se:Hg molar ratio is always higher than 1:1, suggesting that Se is always in excess relative to Hg, therefore not limiting for the detoxification of MeHg. For the liver, kidneys, and muscle, there is a trend of higher Se content with more Hg, which fuels the idea that MeHg is at least partly demethylated by selenolate groups[48,77] in these tissues. The Se and Hg values are somewhat aligned. A regression analysis shows that the Hg and Se concentrations are correlated in the liver ($R^2 = 0.99$). A high Se:Hg ratio is distinctive of the blood (52.2 ± 22.5) and the brain (29.9 ± 18.1). A high Se:Hg ratio in the blood is
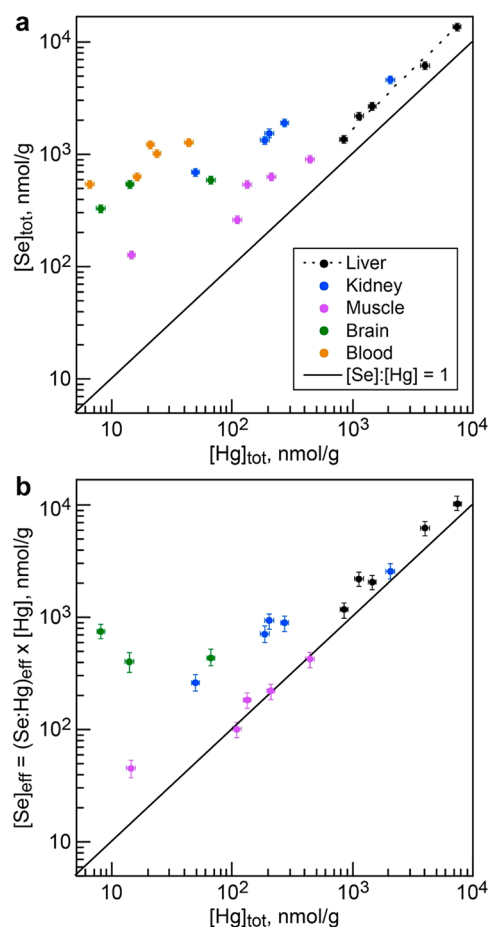

Figure 2. Molar relationship between Hg and Se in the 26 giant petrel tissues analyzed by HR-XANES and straight line corresponding to the 1:1 ratio. (a) Total Se concentration against total Hg concentration in each tissue. Linear-fit of the liver concentrations ($y = −176.1 + 1.83x$, $R^2 = 0.99$). (b) Effective Se concentration against total Hg concentration in each tissue. The Y-axis error bars represent the total propagation of error of the concentrations of Hg and Se and the fractions of Hg species.

consistent with the transport and elimination from the circulatory system of the MeHg species, which has no selenium, and the delivery of essential Se to peripheral tissues. A high Se:Hg ratio in the brain is intriguing because, while the Hg content is lower than in the other organs (5.9 ± 6.4 μg/g), yet the proportion of brain Se to whole-body Se is relatively high (Table S2). The brain has a smaller selenoproteome than the liver and kidneys, being normally similar to that of the muscle.[38] The Se level in brain, as expressed as a percentage of the liver level, is twice that of the Se level in muscle (31.3 ± 9.5 μg/g vs 15.3 ± 8.4 μg/g; Figure 1b). Actually, brain neurons require a reliable supply of selenium for their functioning, as selenium deficiency causes neurological impairment.[33,38,73−76] SelP is delivered to neurons (and endocrine cells) upon binding to the cell-surface apolipoprotein E Receptor-2 (ApoER2).[78,79]

Chemical Forms of Hg. The HR-XANES spectra from the 26 petrel tissues and the EXAFS spectra from eight of them are represented in Figures S1 and S2a. All HR-XANES spectra of feathers were identified as being from a MeHg-cysteinate complex (MeHgCys) and two liver spectra (P1, P2) from HgSe. All other spectra have variable shapes distinct from any standard, implying that they are a weighted sum of single-

species spectra. There is a large inter- and intraindividual variability in tissue speciation, represented in Figures 3a with the brain spectra from individuals P6, P7, and P8, and in Figure 3b with the liver, kidneys, and muscle spectra from a same individual (P2). The compositional variability is also observed on EXAFS spectra (Figure S2b). Investigating all 26 HR-XANES spectra using PCA, we found that four principal components (species) were required to account for the variance in the data set (Figure S3). The single-species spectra needed to describe quantitatively the HR-XANES data set, as identified by target transformation, are shown in Figure 3c−f together with the structure of the Hg species.

Besides MeHgCys and HgSe, two inorganic Hg complexes were identified, a dithiolate $(Hg(SR)_2)$ and a tetraselenolate $(Hg(SeR)_4)$ complex. Since the two complexes occur in biological matter, the thiolate group is from a cysteine residue $(Hg(Cys)_2)$ and the selenolate group from a selenocysteine group $(Hg(Sec)_4)$. The spectrum from the dicysteinate complex $Hg(GSH)_2$ at physiological pH[55] provided the best reconstruction by target transformation for the first complex $(NSS = 1.5 \times 10^{-4})$, and the $Hg(Sec)_4$ spectrum[43] provided the best reconstruction for the second complex $(NSS = 4.8 \times 10^{-5})$. Consideration of the $Hg(Sec)_4$ complex is also needed to explain the variability of the EXAFS spectra (Figure S2b). In $Hg(GSH)_2$, Hg is coordinated primarily to two cysteine residues and secondarily to two oxygen atoms in a seesaw geometry,[59] also denominated disphenoidal (Figure 3). The $Hg[(Cys)_2+(N/O)_{1-2}]$ coordination has been identified previously in the Clark's grebe (in addition to $Hg(Sec)_4$), fish, earthworm, human hair, and bacteria.[43,54,59,60,62]

The molar proportions, or fractional amount f, of the Hg species in the petrel tissues, as obtained by least-squares fitting of the tissue spectra with linear combinations of the four single-species spectra identified by PCA, are given in Table S2. The tissue proportion of each Hg species, averaged over the petrel individuals, is represented in the diagram of Figure 4. The weight concentrations of the Hg species are obtained by multiplying f by the Hg concentration. The main results from the HR-XANES and EXAFS analysis are the following:

- MeHgCys occurs in all tissues, except the liver (detection limit 3% of total Hg). Its proportion decreases in the following order: feathers (100%, $n = 5$) > blood ($83 \pm 20\%$, $n = 3$) > brain ($45 \pm 35\%$, $n = 3$) > kidneys ($4 \pm 5\%$, $n = 5$) = muscle ($4 \pm 5\%$, $n = 5$).

- HgSe and $Hg(Sec)_4$ occur in all tissues, except the feathers and blood (detection limit 9% of total Hg). The proportion of HgSe decreases in the order: liver ($95 \pm 5\%$, $n = 5$) > kidneys ($61 \pm 8\%$, $n = 5$) > brain ($38 \pm 32\%$, $n = 3$) = muscle ($35 \pm 15\%$, $n = 5$). The proportion of $Hg(Sec)_4$ decreases in the order: muscle ($61 \pm 13\%$, $n = 5$) > kidneys ($35 \pm 10\%$, $n = 5$) > brain ($16 \pm 7\%$, $n = 3$) > liver ($5 \pm 2\%$, $n = 5$).

- MeHgCys and HgSe never co-occur without $Hg(Sec)_4$.

- $Hg(Cys)_2$ (modeled with $Hg(GSH)_2$) occurs in the blood of petrels P3 ($12 \pm 9\%$) and P5 ($39 \pm 8\%$) together with MeHgCys, but not in the blood of petrel P1. The low abundance of $Hg(Cys)_2$ in the data set (2 occurrences out of 26), and relatively low signal-to-noise ratio of its HR-XANES spectrum (Figure S1), explain the poorer reconstruction of the $Hg(GSH)_2$ proxy by target transformation: $NSS = 1.5 \times 10^{-4}$, compared to $NSS = 1.4 \times 10^{-6}$ for HgSe, $NSS = 4.8 \times 10^{-5}$ for
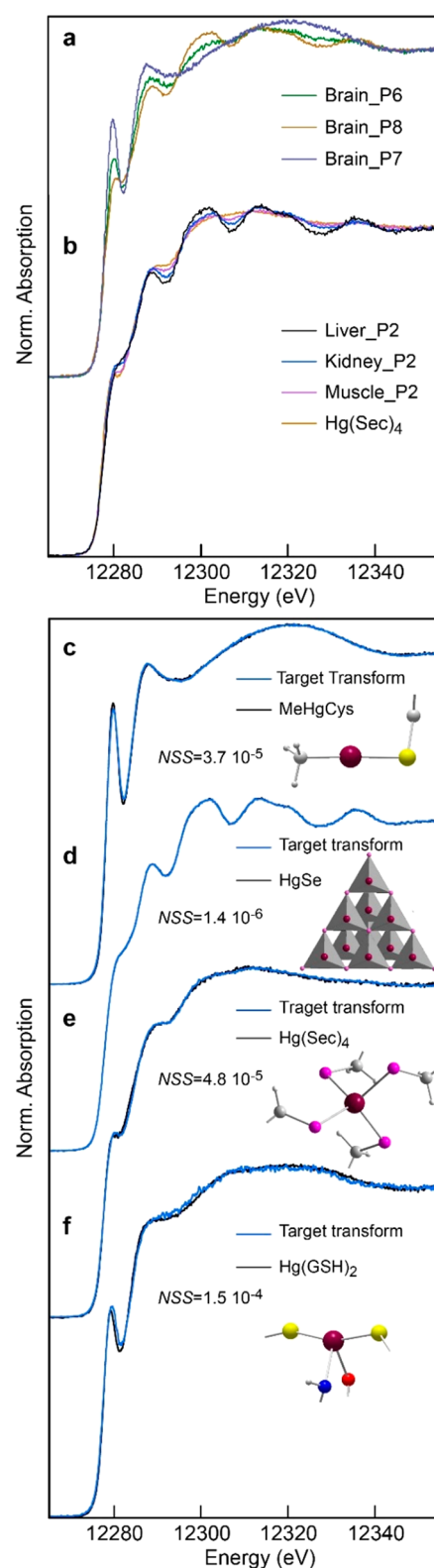
Figure 3. Chemical forms of Hg in tissues of giant petrels derived from Hg L_3-edge HR-XANES spectroscopy. (a) Spectra from the brain of individuals P6, P7, and P8 showing the large interindividual variability in Hg speciation. (b) Spectra from the liver, kidneys, and muscle of the same individual (P2) with the $Hg(Sec)_4$ spectrum showing the tissular variability in Hg speciation. The kidneys and muscle spectra are intermediate between the liver (100% HgSe) and the $Hg(Sec)_4$ spectra, indicating that they contain different amounts of the two species. (c−f) Hg species identified by principal

Figure 3. continued

component analysis of 26 tissue spectra and target transformation of HR-XANES spectra from a library of model compounds and natural species. The MeHgCys spectrum is from Clark's grebe feather and the $Hg(Sec)_4$ spectrum is from Clark's grebe liver.[43] The $Hg(GSH)_2$ spectrum is from ref 59. The Hg[Me+Cys], $Hg[(Sec)_4]$, and $Hg[(Cys)_2+(N/O)_{1-2}]$ coordinations of the Hg complexes are represented in ball-and-stick in the insets and the HgSe structure is represented with corner-linked $Hg(Se)_4$ tetrahedra. For experimental details and data analysis, see the SI.

     $Hg(Sec)_4$, and NSS = 3.7×10^{-5} for MeHgCys (Figure 3c−f).

- The HgSe grains do not contain sulfur, therefore do not form a $Hg(Se_xS_{1-x})$ solid-solution, in contrast to previous hypotheses[22,80] (Figure S4, Table S3).

Imaging of HgSe Nanoparticles. Sparsely distributed electron-dense aggregates of 5 nm up to 100 nm HgSe nanocrystals were imaged, for the first time in seabird tissues, using electron microscopy (Figures 5 and S5−S13). Although large variations in crystal size were observed in each tissue, overall it decreased with the Hg concentration from about 40−100 nm in liver (1499 μg Hg/g dw), to 5−20 nm in kidneys (414 μg Hg/g), to ~3 nm in muscle (88.7 μg Hg/g). Few aggregates of ~3 nm and larger crystals also were observed in the liver. Summation of the EDX spectra from all individual pixels of the large crystal shown in Figure 5a gave an Hg:Se atomic ratio of ~1. The sulfur intensity profile did not increase over the grain compared to the surrounding tissue, negating a

Hg(Se,S) solid solution (Figure S5). The electron diffraction (SAED) pattern and interplanar distances obtained by fast-Fourier transform (FFT) matched the $Fd3m$ cubic space group and a = 6.08 Å lattice dimension of HgSe,[81] which is isostructural to β-HgS (Figure 5a). Crystallographic data and nanochemical analyses performed on many nanocrystals of varying size in the three tissues were all consistent with HgSe. The smallest crystals having lattice planes which could be imaged had a dimension of 4−5 nm. However, STEM imaging of kidney and muscle aggregates show that they contain vanishingly small particles, down to about 1 nm, and perhaps below. The EDX signal from the small particles was too low to measure their Hg:Se ratio.

■ DISCUSSION

This study provides the first evidence in seabird tissues of the $Hg(Sec)_4$ species identified recently in Clark's grebe and freshwater fish.[43] This finding warrants further discussion on its significance for the Hg−Se antagonism, the Se metabolism, and the demethylation of methylmercury as HgSe.

Hg−Se Antagonism. When Hg is bound in equimolar stoichiometry with Se as in HgSe, the Hg:Se atomic ratio derived from chemical analysis (($Hg:Se)_{chem}$) represents the fraction of Se, to total Se, bound to Hg. However, when Hg is complexed to four selenolate ligands, forming a $Hg(Sec)_4$ complex, the effective fraction of Se bound to Hg is higher than the chemical fraction (($Hg:Se)_{eff}$ > ($Hg:Se)_{chem}$). The difference between the two molar ratios depends on the fractional amount, or proportion, of $Hg(Sec)_4$ and HgSe in the
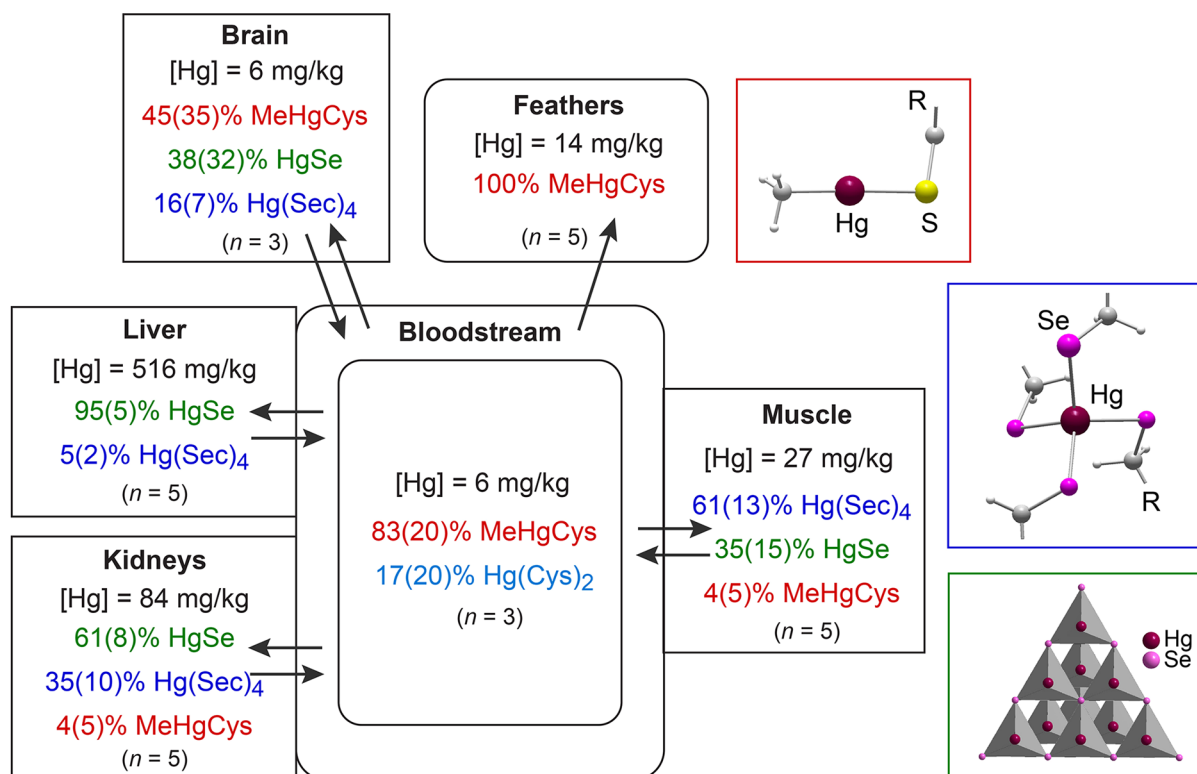
Figure 4. Diagrammatic picture of the average concentration and speciation of Hg in giant petrel tissues. Cys and Sec stand for cysteine and selenocysteine residues within a polymeric chain of peptide or protein, not for free amino acids. Molar percentages and Hg concentrations are mean values over three (blood, brain) and five (liver, kidneys, muscle, feathers) individuals. The numbers in parentheses are the standard deviations. HgSe is most abundant in liver and $Hg(Sec)_4$ is most abundant in muscle.

Figure 5. EDX maps of Hg (green) and Se (red) and transmission electron microscopy images of HgSe nanoparticles in the liver, kidney, and muscle tissues of individual P4. (a) EDX map and HRTEM image of two large HgSe crysta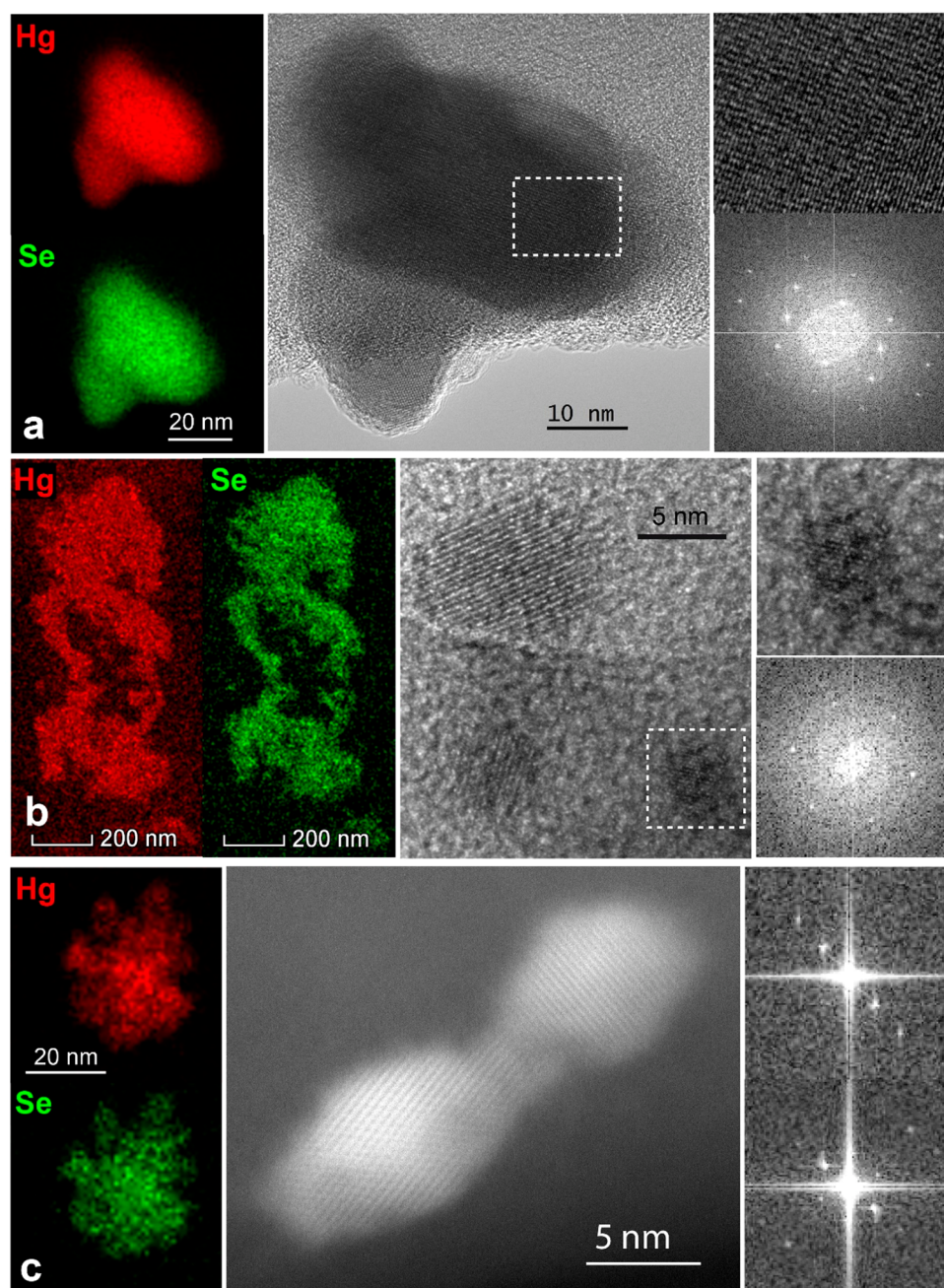ls in liver. The upper image on the right is a magnification of the framed area and the lower image is its fast Fourier transform (FFT) image. The FFT pattern corresponds to the [112] zone axis of HgSe with a = 6.08 Å. (b) EDX map of an aggregate of HgSe nanoparticles and HRTEM image of three small 4 to 10 nm HgSe crystals in kidney. The framed area is enlarged on the upper right and Fourier transformed on the lower right. (c) EDX map of an aggregate of HgSe nanoparticles in the muscle, and STEM image from 25 drift-corrected individual frames of two nanocrystals and corresponding FFT images of the upper and lower grains, respectively. This STEM image was recorded at −170 °C and 60 pA electron current to minimize radiation damage.

sample, noted $f_{Hg(Sec)4}$ and f_{HgSe}. The effective Hg:Se ratio can be written as follows:

$$(\text{Hg:Se})_{eff} = (\text{Hg:Se})_{chem} \times (f_{HgSe} + 4 \times f_{Hg(Sec)4})$$

For example, the liver of petrel P3 has $(\text{Hg:Se})_{chem}$ = 0.54, f_{HgSe} = 0.91, $f_{Hg(Sec)4}$ = 0.09, which gives $(\text{Hg:Se})_{eff}$ = 0.69. The concentration of bioavailable Se is $[\text{Se}]_{bio} = (1 - (\text{Hg:Se})_{eff}) \times [\text{Se}]_{tot}$. In this example, $[\text{Se}]_{tot}$ = 213 μg/g and $[\text{Se}]_{bio}$ = 66 μg/g (Table S2). Omitting the 1:4 stoichiometric ratio of $Hg(Sec)_4$ gives an apparent concentration of $[\text{Se}]_{bio}^{app} = (1-$

0.54) × 213 = 98 μg/g, 48% higher than the actual concentration. Similarly, the kidney tissue of petrel P4 have $[\text{Se}]_{tot}$ = 363 μg/g, $[\text{Se}]_{bio}^{app} = (1-0.45) \times 363 = 200$ μg/g, and $[\text{Se}]_{bio}$ = 58 μg/g. The apparent excess of Se obtained by omitting the $Hg(Sec)_4$ complex is more than three times higher than the actual value. Overestimating $[\text{Se}]_{bio}$ is not a key issue in liver and kidneys as Se concentration is not limiting in these tissues. In contrast, overestimating $[\text{Se}]_{bio}$ leads to underestimate the toxicological risk for muscle, as discussed below.

The relationships between $(Hg:Se)_{chem}$ and $[Hg]_{tot}$ and between $(Hg:Se)_{eff}$ and $[Hg]_{tot}$ in the 26 tissues are shown in Figure 6a,b, and the fraction of bioavailable Se to total Se
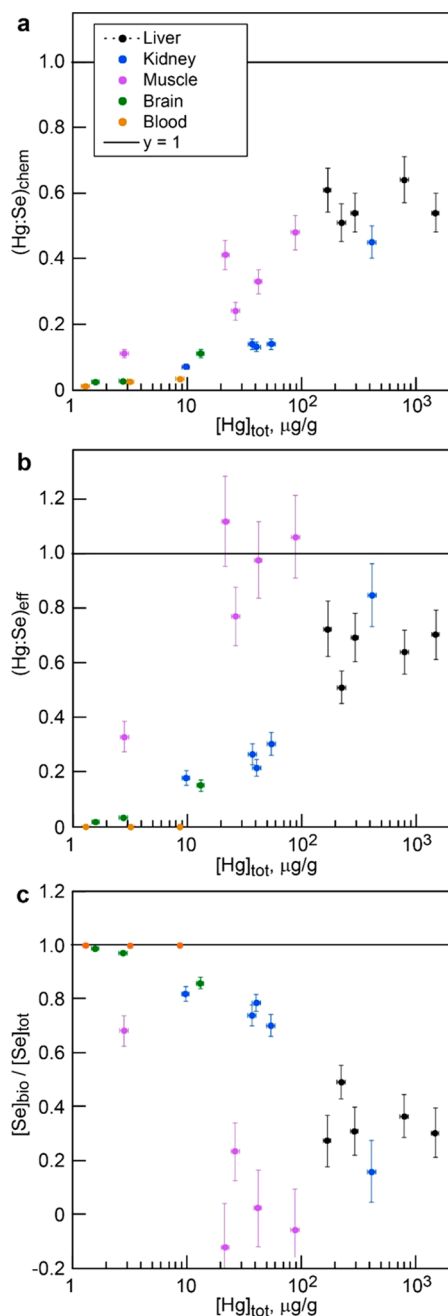

Figure 6. Chemical (a) and effective (b) fractions of Se bound to Hg against total Hg concentration in each tissue. (c) Fraction of bioavailable to total Se against total Hg concentration in each tissue. The Y-axis error bars represent the total propagation of errors from chemical analysis and HR-XANES least-squares fits.

$([Se]_{bio}/[Se]_{tot})$ in Figure 6c. Molar Hg:Se ratios vary greatly among all tissues and between individuals as shown previously in Figure 2a. Incorporating $f_{Hg(Sec)4}$ in the calculation of Hg:Se has the most effect on the muscular tissue. In three out of five birds (P2, P3, P4), muscular $(Hg:Se)_{eff}$ is close to 1:1 (Figure 6b), the threshold from which toxic effects may emerge.[37] The accuracy on ratios is highly variable, however, as a result of the propagation of uncertainties from chemical analyses and

spectroscopic values of f_{HgSe} and $f_{Hg(Sec)4}$. Notwithstanding these cumulative errors, it appears clearly that the muscle is the most affected of all tissues by Hg contamination. For example, the muscle of petrel P2 has a few $\mu g/g$ of bioavailable Se at most, for an apparent concentration of $[Se]_{bio}^{app} = (1-0.33) \times 50.8 = 34 \ \mu g/g$ (Table S2).

Figure 2a also can be corrected for $f_{Hg(Sec)4}$ like Figure 6a. In this case $[Se]_{tot}$ on the y-scale needs to be replaced by the effective Se concentration, which is as follows:

$$[Se]_{eff} = (1/(Hg:Se)_{eff}) \times [Hg]_{tot} = (Se:Hg)_{eff} \times [Hg]_{tot}$$

with $[Hg]_{tot}$ and $[Se]_{eff}$ in mol/g. In this representation, the muscle tissues of the three birds that are depleted in bioavailable Se (P2, P3, P4) are aligned on the 1:1 theoretical line (Figure 2b). Blood results cannot be represented on this graph because Hg is not bound to Se, but is in methylated and dicysteinate form only $(MeHgCys + Hg(Cys)_2)$. For this tissue, the $(Se:Hg)_{eff}$ ratio, which represents the excess of Se, is infinite.

Se Metabolism. Selenium is an essential element which is distributed by the liver to nonhepatic tissues to maintain Se homeostasis.[33,38] Selenium content is well-regulated in laboratory animals fed with dietary Se intakes. In mice, the regulated selenium pool is about 200 ng/g wet weight (~1 $\mu g/$ g dw) in muscle and 1500 ng/g wet weight (~6 $\mu g/g$ dw) in liver.[82] As intake increases, excess Se is excreted predominantly via urine. The bioavailable concentration of Se in the muscle of the three most depleted birds (P2, P3, P4) is on the order of 1 ± 10 $\mu g/g$ dw (i.e., 0.1–10 $\mu g/g$). Although muscular tissues are most impacted by Hg contamination, a Hg-induced Se-deficiency is unlikely because the liver contains enough bioavailable Se for replenishment (Figure S14a). The liver of the two most contaminated birds (P2, P4), containing 804 $\mu g/$ g and 1499 μg Hg/g dw, respectively, are concomitantly in tremendous excess of $[Se]_{bio}$ (Figure S14b). The $[Se]_{bio}:[Se]_{tot}$ ratio is approximately constant ranging between 0.28 and 0.49 (Figure S14c).

Source of the Hg–Dicysteinate Species. The $Hg(Cys)_2$ species was detected in the blood of individuals P3 and P5, not P1, and co-occurs with MeHgCys. The source of MeHg is clearly exogenous since it is the main form of Hg in the preys of petrel, such as fish and squids,[83−86] and is almost totally (90−95%) absorbed in the gastrointestinal tract.[87,88] The $Hg(Cys)_2$ species is probably exogenous too, otherwise Hg would be bonded to Se, not to S, as no MeHgCys to $Hg(Cys)_2$ demethylation pathway is known in the body to date. Gastrointestinal absorption of $Hg(Cys)_2$, although inefficient (7−15%), occurs in the lumen of the intestine.[89,90] $Hg(Cys)_2$ can be produced by demethylating intestinal microflora or taken up through the diet. Giant petrels eat fish and cephalopods when they are at sea and they are very aggressive predators and scavengers of mammal's and bird's carcasses when on land. The high variation of the $\%Hg(Cys)_2$ to % MeHgCys ratio in blood among the three birds (P1:0%/100%; P3:12%/88%; P5:39%/61%) argues for a dietary source that differed at the time of sampling. Thus, Hg speciation in blood informs about recent intakes. The lack of $Hg(Cys)_2$ in other tissues can be explained by a Se for S ligand exchange and by its elimination from the bloodstream in urine.[91]

Demethylation of Methylmercury. It has been suggested that the HgSe demethylation reaction is a concentration-sensitive process in the liver of dolphins and waterbirds, starting when a Hg concentration threshold is reached.[92,93] In

waterbirds the threshold value is approximately 8.5 μg Hg/g dw. Here, there is no evidence for a demethylation threshold because the liver concentrations are at least 20 times higher than the waterbird threshold ($[Hg]_{tot} > 170$ μg/g). Because the vast majority of Hg is inorganic and %HgSe $\geq 90 \pm 6\%$, quantities of MeHg are very low (Table S2). In contrast to liver, there is some supporting evidence for a HgSe threshold in brain, as its Hg concentration ranges from 1.6 μg/g (petrel P7) to 13.2 μg/g (P8). The response of %MeHg to changing brain $[Hg]_{tot}$ is strongly curvilinear (Figure S14c).%MeHg declines abruptly from $83 \pm 5\%$ at $[Hg]_{tot} = 1.6$ μg/g, to $40 \pm 6\%$ at $[Hg]_{tot} = 2.8$ μg/g, and then less rapidly to $13 \pm 5\%$ at $[Hg]_{tot} = 13.2$ μg/g. In contrast, %HgSe and %(HgSe +Hg(Sec)$_4$) follow a power-law with $[Hg]_{tot}$. HgSe amounts to $8 \pm 8\%$ at $[Hg]_{tot} = 1.6$ μg/g, $36 \pm 13\%$ at $[Hg]_{tot} = 2.8$ μg/g, and $71 \pm 8\%$ at $[Hg]_{tot} = 13.2$ μg/g (Table S2, Figure S14d). This suggests that (1) brain MeHg accumulates to a threshold concentration of about 1−2 μg/g above which HgSe is formed, and (2) HgSe nucleation is initiated by the Hg(Sec)$_4$ complex, in agreement with electron microscopy observations and previous results on the Clark's grebe.[43] The fact that MeHgCys and HgSe never coexist in any tissue without Hg(Sec)$_4$ is another supporting line of evidence for Hg(Sec)$_4$ being an intermediate species of the demethylation reaction. Hg(Sec)$_4$ observed in kidneys, muscle, and brain may be transported from the liver since Hg-bound SelP has been detected in the plasma of humans.[46,47] Hg(Sec)$_4$ may also form in situ from MeHgCys and SelP delivered by the bloodstream, and from SelP directly produced in peripheral tissues.[76,94]

The low demethylation threshold value observed in the brain, together with a $[Se]_{tot}/[Hg]_{tot}$ molar ratio of 30 ± 18 (Figure 2a), many times higher than that in the other tissues, suggest that the brain is the first organ protected from injury. This finding agrees with Se-deficiency experiments on animal models, which show that neurons take up Se via the ApoER2 receptor at the expense of kidneys and muscle to prevent injury.[38,73,76] Demethylation of MeHg in HgSe has been observed previously in the brains of dolphins[26] and humans.[95]

Molecular Structure of the Hg−Tetraselenolate Complex. We showed recently that the Hg(Sec)$_4$ complex is bound to selenoprotein P in the Clark's grebe.[43] SelP is present in all vertebrates and harbors at least ten Sec residues, compared to at most two in other selenoproteins.[96] Birds have one Sec in the α-domain and 12 in the β-domain, seven of which being grouped in the carboxyl-terminus region of the protein.[43] The last four Sec residues of the protein tail are arranged in the highly conserved amino acid motif XUXUX^{6}UXUX (single-letter amino acid code, where U is Sec and X can be any amino acid). With its four Sec residues, this region is the most likely Hg-binding site. The tertiary structure of the predicted Hg-binding site in giant petrel was modeled by iterative threading assembly refinement (I-TASSER[97,98]) from the amino acid sequence of the northern fulmar (*Fulmarus glacialis*). I-TASSER matches with Monte Carlo simulations the structure of 3D models with known protein structures in the Protein Data Bank (PDB). SelP of giant petrel has not been sequenced, but it should be close to that of northern fulmar, as it is phylogenetically close (both belong to the fulmarine group within the same Procellariidae family). The two UXU motifs are predicted to face each other on each side of a β-turn, forming a four-coordinate metal-binding site (Figure 7).
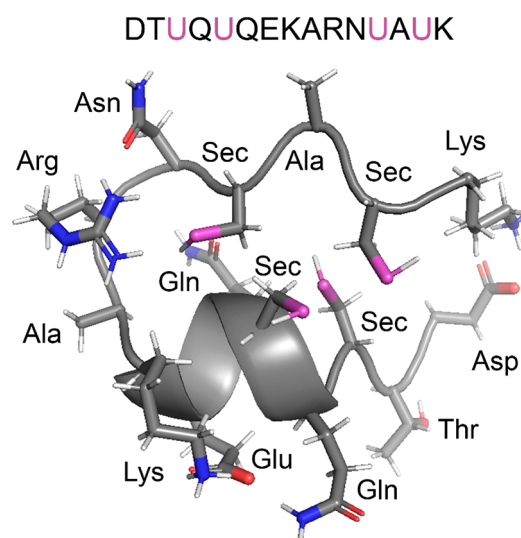

Figure 7. Ribbon representation of the predicted tertiary structure from I-Tasser[97,98] of the carboxyl-terminus region of selenoprotein P for northern fulmar (*Fulmarus glacialis*), as a proxy for giant petrel. Purple: Se atoms, blue: N atoms, red: O atoms from the amino acid side chains attached to the protein backbone in gray. The β-turn forms a molecular cage with four selenolate ligands pointing out at the surface of the loop. This cage is a potential binding site for Hg. The amino acid sequence is represented in both single-letter and triple-letter code. U is the single-letter code for selenocysteine. The structure was visualized with PyMol.[105]

The association in Hg−Se aggregates of <4 nm nano-particles with $\geq$4 nm HgSe crystals (Figures S10, S11, and S13) is suggestive of a continuum of Hg cluster sizes from Hg$_x$(Se,Sec)$_y$ multinuclear complexes to HgSe nanocrystals. We hypothesize that the flexible Sec-rich β-domain of SelP forms a multinuclear binding pocket via protein folding and mediates the biomineralization of HgSe via self-assembling. This mechanism is common in the biosynthesis of metal-loclusters,[99−101] and is reminiscent of metal clustering in metallothioneins.[56,102,103] Then, the Hg(Sec)$_4$ complex would act as an external ligand to the nascent HgSe nanoparticles, decreasing their Hg:Se molar ratio below 1. Supporting this possibility is the deviation of the equimolar ratio observed near HgSe grains in the liver of dolphins by Gajdosechova and co-workers.[26] We considered all along this study that the Hg(Sec)$_4$ complex is mononuclear. If the β-domains of SelP host multinuclear Hg$_x$(Se,Sec)$_y$ complexes, then they would be too disordered to be identified as a distinct species by HR-XANES. A caveat in assigning all tetraselenolate complexes to Hg(Sec)$_4$ is an overestimation of (Hg:Se)$_{eff}$, because $y < 4x$ in Hg$_x$(Se,Sec)$_y$.[43] We also considered in this study that Hg is the only potent electrophile capable of binding Se. However, there are additional elements of environmental concern which can also bind it and contribute to loss of Se that is biologically available for selenoenzyme synthesis. Organic electro-philes[33,104] bioaccumulated in polluted ecosystems may contribute to impair Se bioavailability.

■ ASSOCIATED CONTENT

ⓢ Supporting Information

The Supporting Information is available free of charge at https://pubs.acs.org/doi/10.1021/acs.est.0c06269.

Materials, methods, data analysis, supplementary tables, and figures (PDF)

HR-XANES spectra (XLSX)

■ AUTHOR INFORMATION

Corresponding Author

    Alain Manceau − *Université Grenoble Alpes, CNRS, ISTerre, 38000 Grenoble, France;* ◎ orcid.org/0000-0003-0845-611X; Email: alain.manceau@univ-grenoble-alpes.fr

Authors

    Anne-Claire Gaillot − *Université Nantes, CNRS, Institut des Matériaux Jean Rouxel, IMN, 44000 Nantes, France*

    Pieter Glatzel − *European Synchrotron Radiation Facility (ESRF), 38000 Grenoble, France;* ◎ orcid.org/0000-0001-6532-8144

    Yves Cherel − *Centre d'Etudes Biologiques de Chizé (CEBC), CNRS−La Rochelle Université, 79360 Villiers-en-Bois, France*

    Paco Bustamante − *La Rochelle Université, CNRS, Littoral Environnement et Sociétés (LIENSs), 17000 La Rochelle, France;* ◎ orcid.org/0000-0003-3877-9390

Complete contact information is available at:
https://pubs.acs.org/10.1021/acs.est.0c06269

Notes

The authors declare no competing financial interest.

■ REFERENCES

(1) Gonzalez-Solis, J.; Sanpera, C.; Ruiz, X. Metals and selenium as bioindicators of geographic and trophic segregation in giant petrels *Macronectes* spp. *Mar. Ecol.: Prog. Ser.* **2002**, *244*, 257−264.

(2) Carvalho, P. C.; Bugoni, L.; McGill, R. A. R.; Bianchini, A. Metal and selenium concentrations in blood and feathers of petrels of the genus procellaria. *Environ. Toxicol. Chem.* **2013**, *32*, 1641−1648.

(3) Bustamante, P.; Carravieri, A.; Goutte, A.; Barbraud, C.; Delord, K.; Chastel, O.; Weimerskirch, H.; Cherel, Y. High feather mercury concentrations in the wandering albatross are related to sex, breeding status and trophic ecology with no demographic consequences. *Environ. Res.* **2016**, *144*, 1−10.

(4) Carravieri, A.; Cherel, Y.; Brault-Favrou, M.; Churlaud, C.; Peluhet, L.; Labadie, P.; Budzinski, H.; Chastel, O.; Bustamante, P. From Antarctica to the subtropics: Contrasted geographical concentrations of selenium, mercury, and persistent organic pollutants in skua chicks (*Catharacta* spp.). *Environ. Pollut.* **2017**, *228*, 464−473.

(5) Sebastiano, M.; Bustamante, P.; Eulaers, I.; Malarvannan, G.; Mendez-Fernandez, P.; Churlaud, C.; Blevin, P.; Hauselmann, A.; Covaci, A.; Eens, M.; Costantini, D.; Chastel, O. Trophic ecology drives contaminant concentrations within a tropical seabird community. *Environ. Pollut.* **2017**, *227*, 183−193.

(6) Albert, C.; Renedo, M.; Bustamante, P.; Fort, J. Using blood and feathers to investigate large-scale Hg contamination in Arctic seabirds: A review. *Environ. Res.* **2019**, *177*, 108588.

(7) Gilmour, M. E.; Lavers, J. L.; Lamborg, C.; Chastel, O.; Kania, S. A.; Shaffer, S. A. Mercury as an indicator of foraging ecology but not the breeding hormone prolactin in seabirds. *Ecol. Indic.* **2019**, *103*, 248−259.

(8) Renedo, M.; Pedrero, Z.; Amouroux, D.; Cherel, Y.; Bustamante, P. Mercury isotopes of key tissues document mercury metabolic processes in seabirds. *Chemosphere* **2021**, *263*, 127777.

(9) Norheim, G. Levels and interactions of heavy-metals in sea birds from Svalbard and the Antarctic. *Environ. Pollut.* **1987**, *47*, 83−94.

(10) Kim, E. Y.; Goto, R.; Tanabe, S.; Tanaka, H.; Tatsukawa, R. Distribution of 14 elements in tissues and organs of oceanic seabirds. *Arch. Environ. Contam. Toxicol.* **1998**, *35*, 638−645.

(11) Ikemoto, T.; Kunito, T.; Tanaka, H.; Baba, N.; Miyazaki, N.; Tanabe, S. Detoxification mechanism of heavy metals in marine mammals and seabirds: Interaction of selenium with mercury, silver, copper, zinc, and cadmium in liver. *Arch. Environ. Contam. Toxicol.* **2004**, *47* (3), 402−413.

(12) Burger, J.; Jehl, J. R.; Gochfeld, M. Selenium:mercury molar ratio in eared grebes (*Podiceps nigricollis*) as a possible biomarker of exposure. *Ecol. Indic.* **2013**, *34*, 60−68.

(13) Cipro, C. V. Z.; Cherel, Y.; Caurant, F.; Miramand, P.; Mendez-Fernandez, P.; Bustamante, P. Trace elements in tissues of white-chinned petrels (*Procellaria aequinoctialis*) from Kerguelen waters, Southern Indian Ocean. *Polar Biol.* **2014**, *37*, 763−771.

(14) Moura, J. F.; Tavares, D. C.; Lemos, L. S.; Acevedo-Trejos, E.; Saint'Pierre, T. D.; Siciliano, S.; Merico, A. Interspecific variation of essential and non-essential trace elements in sympatric seabirds. *Environ. Pollut.* **2018**, *242*, 470−479.

(15) Melnick, J. G.; Yurkerwich, K.; Parkin, G. On the chalcogenophilicity of mercury: Evidence for a strong Hg-Se bond in [Tm^{But}]HgSePh and its relevance to the toxicity of mercury. *J. Am. Chem. Soc.* **2010**, *132*, 647−655.

(16) Ohi, G.; Nishigaki, S.; Seki, H.; Tamura, Y.; Maki, T.; Konno, H.; Ochiai, S.; Yamada, H.; Shimamura, Y.; Mizoguchi, I.; Yagyu, H. Efficacy of selenium in tuna and selenite in modifying methylmercury intoxication. *Environ. Res.* **1976**, *12* (1), 49−58.

(17) Dauplais, M.; Lazard, M.; Blanquet, S.; Plateau, P. Neutralization by metal ions of the toxicity of sodium selenide. *PLoS One* **2013**, *8*, No. e54353.

(18) Gailer, J.; George, G. N.; Pickering, I. J.; Madden, S.; Prince, R. C.; Yu, E. Y.; Denton, M. B.; Younis, H. S.; Aposhian, H. V. Structural basis of the antagonism between inorganic mercury and selenium in mammals. *Chem. Res. Toxicol.* **2000**, *13*, 1135−1142.

(19) Cuvin-Aralar, M. L. A.; Furness, R. W. Mercury and selenium interaction: a review. *Ecotoxicol. Environ. Saf.* **1991**, *21*, 348−364.

(20) Yang, D. Y.; Chen, Y. W.; Gunn, J. M.; Belzile, N. Selenium and mercury in organisms: Interactions and mechanisms. *Environ. Rev.* **2008**, *16*, 71−92.

(21) Li, M. L.; Juang, C. A.; Ewald, J. D.; Yin, R. S.; Mikkelsen, B.; Krabbenhoft, D. P.; Balcom, P. H.; Dassuncao, C.; Sunderland, E. M. Selenium and stable mercury isotopes provide new insights into mercury toxicokinetics in pilot whales. *Sci. Total Environ.* **2020**, *710*, 136325.

(22) Arai, T.; Ikemoto, T.; Hokura, A.; Terada, Y.; Kunito, T.; Tanabe, S.; Nakai, I. Chemical forms of mercury and cadmium accumulated in marine mammals and seabirds as determined by XAFS analysis. *Environ. Sci. Technol.* **2004**, *38*, 6468−6474.

(23) Nakazawa, E.; Ikemoto, T.; Hokura, A.; Terada, Y.; Kunito, T.; Tanabe, S.; Nakai, I. The presence of mercury selenide in various tissues of the striped dolphin: evidence from *μ*-XRF-XRD and XAFS analyses. *Metallomics* **2011**, *3*, 719−725.

(24) Lailson-Brito, J.; Cruz, R.; Dorneles, P. R.; Andrade, L.; Azevedo, A. D.; Fragoso, A. B.; Vidal, L. G.; Costa, M. B.; Bisi, T. L.; Almeida, R.; et al. Mercury-selenium relationships in liver of Guiana

dolphin: The possible role of Kupffer cells in the detoxification process by tiemannite formation. *PLoS One* **2012**, *7*, No. e42162.

(25) Sakamoto, M.; Itai, T.; Yasutake, A.; Iwasaki, T.; Yasunaga, G.; Fujise, Y.; Nakamura, M.; Murata, K.; Chan, H. M.; Domingo, J. L.; et al. Mercury speciation and selenium in toothed-whale muscles. *Environ. Res.* **2015**, *143*, 55−61.

(26) Gajdosechova, Z.; Lawan, M. M.; Urgast, D. S.; Raab, A.; Scheckel, K. G.; Lombi, E.; Kopittke, P. M.; Loeschner, K.; Larsen, E. H.; Woods, G.; et al. In vivo formation of natural HgSe nanoparticles in the liver and brain of pilot whales. *Sci. Rep.* **2016**, *6*, 34361.

(27) Huggins, F. E.; Raverty, S. A.; Nielsen, O. S.; Sharp, N. E.; Robertson, J. D.; Ralston, N. V. C. An XAFS investigation of mercury and selenium in Beluga whale tissues. *Environ. Bioindic.* **2009**, *4*, 291−302.

(28) Khan, M. A. K.; Wang, F. Y. Chemical demethylation of methylmercury by selenoamino acids. *Chem. Res. Toxicol.* **2010**, *23*, 1202−1206.

(29) Ralston, N. V. C.; Blackwell, J. L.; Raymond, L. J. Importance of molar ratios in selenium-dependent protection against methyl-mercury toxicity. *Biol. Trace Elem. Res.* **2007**, *119*, 255−268.

(30) Peterson, S. A.; Ralston, N. V. C.; Peck, D. V.; Van Sickle, J.; Robertson, J. D.; Spate, V. L.; Morris, J. S. How might selenium moderate the toxic effects of mercury in stream fish of the western US? *Environ. Sci. Technol.* **2009**, *43*, 3919−3925.

(31) Sormo, E. G.; Ciesielski, T. M.; Overjordet, I. B.; Lierhagen, S.; Eggen, G. S.; Berg, T.; Jenssen, B. M. Selenium moderates mercury toxicity in free-ranging freshwater fish. *Environ. Sci. Technol.* **2011**, *45*, 6561−6566.

(32) Kehrig, H. A.; Seixas, T. G.; Di Beneditto, A. P. M.; Malm, O. Selenium and mercury in widely consumed seafood from South Atlantic Ocean. *Ecotoxicol. Environ. Saf.* **2013**, *93*, 156−162.

(33) Ralston, N. V. C.; Raymond, L. J. Mercury's neurotoxicity is characterized by its disruption of selenium biochemistry. *Biochim. Biophys. Acta, Gen. Subj.* **2018**, *1862* (11), 2405−2416.

(34) Yu, X. P.; Wang, M. X.; Nan, X. J.; Guo, Y. F.; Deng, T. L. Species and correlations between selenium and mercury in fishpond ecosystems. *Water Environ. Res.* **2019**, *91*, 292−299.

(35) Ralston, N. V. C.; Ralston, C. R.; Blackwell, J. L.; Raymond, L. J. Dietary and tissue selenium in relation to methylmercury toxicity. *NeuroToxicology* **2008**, *29*, 802−811.

(36) Calatayud, M.; Devesa, V.; Virseda, J. R.; Barbera, R.; Montoro, R.; Velez, D. Mercury and selenium in fish and shellfish: Occurrence, bioaccessibility and uptake by Caco-2 cells. *Food Chem. Toxicol.* **2012**, *50* (8), 2696−2702.

(37) Mulder, P. J.; Lie, E.; Eggen, G. S.; Ciesielski, T. M.; Berg, T.; Skaare, J. U.; Jenssen, B. M.; Sormo, E. G. Mercury in molar excess of selenium interferes with thyroid hormone function in free-ranging freshwater fish. *Environ. Sci. Technol.* **2012**, *46*, 9027−9037.

(38) Burk, R. F.; Hill, K. E. Regulation of selenium metabolism and transport. In *Annu. Rev. Nutr.*; Bowman, B. A.; Stover, P. J., Eds.; 2015; Vol. 35, pp 109−134.

(39) Falnoga, I.; Tusek-Znidaric, M.; Stegnar, P. The influence of long-term mercury exposure on selenium availability in tissues: An evaluation of data. *BioMetals* **2006**, *19*, 283−294.

(40) Cusack, L. K.; Eagles-Smith, C.; Harding, A. K.; Kile, M.; Stone, D. Selenium: mercury molar ratios in freshwater fish in the Columbia River basin: Potential applications for specific fish consumption advisories. *Biol. Trace Elem. Res.* **2017**, *178*, 136−146.

(41) Zhang, H.; Feng, X. B.; Chan, H. M.; Larssen, T. New insights into traditional health risk assessments of mercury exposure: Implications of selenium. *Environ. Sci. Technol.* **2014**, *48*, 1206−1212.

(42) Yamashita, M.; Yamashita, Y.; Suzuki, T.; Kani, Y.; Mizusawa, N.; Imamura, S.; Takemoto, K.; Hara, T.; Hossain, M. A.; Yabu, T.; Touhata, K. Selenoneine, a novel selenium-containing compound, mediates detoxification mechanisms against methylmercury. Accumu-lation and toxicity in zebrafish embryo. *Mar. Biotechnol.* **2013**, *15*, 559−570.

(43) Manceau, A.; Bourdineaud, J. P.; Oliveira, R. B.; Sarrazin, S. L. F.; Krabbenhoft, D. P.; Eagles-Smith, C. A.; Ackerman, J. T.; Stewart, A. R.; Ward-Deitrich, C.; Busto, M. E. D.; Goenaga-Infante, H.; Wack, A.; Retegan, M.; Detlefs, B.; Glatzel, P.; Bustamante, P.; Nagy, K. L.; Poulin, B. A. Demethylation of methylmercury in bird, fish, and earthworm. *Environ. Sci. Technol.* **2021**. DOI: 10.1021/ac-s.est.0c04948.

(44) Yamashita, Y.; Yamashita, M. Identification of a novel selenium-containing compound, selenoneine, as the predominant chemical form of organic selenium in the blood of bluefin tuna. *J. Biol. Chem.* **2010**, *285*, 18134−18138.

(45) Achouba, A.; Dumas, P.; Ouellet, N.; Little, M.; Lemire, M.; Ayotte, P. Selenoneine is a major selenium species in beluga skin and red blood cells of Inuit from Nunavik. *Chemosphere* **2019**, *229*, 549−558.

(46) Achouba, A.; Dumas, P.; Ouellet, N.; Lemire, M.; Ayotte, P. Plasma levels of selenium-containing proteins in Inuit adults from Nunavik. *Environ. Int.* **2016**, *96*, 8−15.

(47) Chen, C. Y.; Yu, H. W.; Zhao, J. J.; Li, B.; Qu, L. Y.; Liu, S. P.; Zhang, P. Q.; Chai, Z. F. The roles of serum selenium and selenoproteins on mercury toxicity in environmental and occupational exposure. *Environ. Health Perspect.* **2006**, *114*, 297−301.

(48) Palmer, J. H.; Parkin, G. Protolytic cleavage of Hg-C bonds induced by 1-methyl-1,3-dihydro-2H-benzimidazole-2-selone: Syn-thesis and structural characterization of mercury complexes. *J. Am. Chem. Soc.* **2015**, *137*, 4503−4516.

(49) Jalilehvand, F.; Leung, B. O.; Izadifard, M.; Damian, E. Mercury(II) cysteine complexes in alkaline aqueous solution. *Inorg. Chem.* **2006**, *45*, 66−73.

(50) Warner, T.; Jalilehvand, F. Formation of Hg(II) tetrathiolate complexes with cysteine at neutral pH. *Can. J. Chem.* **2016**, *94*, 373.

(51) Nogara, P. A.; Oliveira, C. S.; Schmitz, G. L.; Piquini, P. C.; Farina, M.; Aschner, M.; Rocha, J. B. T., Methylmercury's chemistry: From the environment to the mammalian brain. *Biochim. Biophys. Acta, Gen. Subj.* **2019**, *1863*, 129284.

(52) Manceau, A.; Lemouchi, C.; Enescu, M.; Gaillot, A.-C.; Lanson, M.; Magnin, V.; Glatzel, P.; Poulin, B. A.; Ryan, J. N.; Aiken, G. R.; Gautier-Luneau, I.; Nagy, K. L. Formation of mercury sulfide from Hg(II)-thiolate complexes in natural organic matter. *Environ. Sci. Technol.* **2015**, *49*, 9787−9796.

(53) Manceau, A.; Lemouchi, C.; Rovezzi, M.; Lanson, M.; Glatzel, P.; Nagy, K. L.; Gautier-Luneau, I.; Joly, Y.; Enescu, M. Structure, bonding, and stability of mercury complexes with thiolate and thioether ligands from high-resolution XANES spectroscopy and first-principles calculations. *Inorg. Chem.* **2015**, *54*, 11776−11791.

(54) Manceau, A.; Enescu, M.; Simionovici, A.; Lanson, M.; Gonzalez-Rey, M.; Rovezzi, M.; Tucoulou, R.; Glatzel, P.; Nagy, K. L.; Bourdineaud, J.-P. Chemical forms of mercury in human hair reveal sources of exposure. *Environ. Sci. Technol.* **2016**, *50*, 10721−10729.

(55) Manceau, A.; Wang, J.; Rovezzi, M.; Glatzel, P.; Feng, X. Biogenesis of mercury-sulfur nanoparticles in plant leaves from atmospheric gaseous mercury. *Environ. Sci. Technol.* **2018**, *52*, 3935−3948.

(56) Manceau, A.; Bustamante, P.; Haouz, A.; Bourdineaud, J. P.; Gonzalez-Rey, M.; Lemouchi, C.; Gautier-Luneau, I.; Geertsen, V.; Barruet, E.; Rovezzi, M.; et al. Mercury(II) binding to metallothionein in *Mytilus edulis* revealed by high energy-resolution XANES spectroscopy. *Chem. - Eur. J.* **2019**, *25*, 997−1009.

(57) Manceau, A.; Nagy, K. L. Thiols in natural organic matter: Molecular forms, acidity, and reactivity with mercury(II) from First-Principles calculations and high energy-resolution X-ray absorption near-edge structure spectroscopy. *ACS Earth Space Chem.* **2019**, *3* (12), 2795−2807.

(58) Thomas, S. A.; Catty, P.; Hazemann, J. L.; Michaud-Soret, I.; Gaillard, J. F. The role of cysteine and sulfide in the interplay between microbial Hg(II) uptake and sulfur metabolism. *Metallomics* **2019**, *11* (7), 1219−1229.

(59) Bourdineaud, J.-P.; Gonzalez-Rey, M.; Rovezzi, M.; Glatzel, P.; Nagy, K. L.; Manceau, A. Divalent mercury from dissolved organic

matter is bioavailable to fish and accumulates as dithiolate and tetrathiolate complexes. *Environ. Sci. Technol.* **2019**, *53*, 4880−4891.

(60) Bourdineaud, J. P.; Durn, G.; Režun, B.; Manceau, A.; Hrenović, J. The chemical species of mercury accumulated by *Pseudomonas idrijaensis*, a bacterium from a rock of the Idrija mercury mine, Slovenia. *Chemosphere* **2020**, *248*, 126002.

(61) Thomas, S. A.; Mishra, B.; Myneni, S. C. B. Cellular mercury coordination environment, and not cell surface ligands, influence bacterial methylmercury production. *Environ. Sci. Technol.* **2020**, *54*, 3960−3968.

(62) Manceau, A.; Nagy, K. L.; Glatzel, P.; Bourdineaud, J. P. Molecular and cellular mechanisms of mercury toxicity to bacteria. *Environ. Sci. Technol.* **2021**, in press.

(63) Nagy, K. L.; Manceau, A.; Gasper, J. D.; Ryan, J. N.; Aiken, G. R. Metallothionein-like multinuclear clusters of mercury(II) and sulfur in peat. *Environ. Sci. Technol.* **2011**, *45*, 7298−7306.

(64) George, G. N.; Pickering, I. J.; Pushie, M. J.; Nienaber, K.; Hackett, M. J.; Ascone, I.; Hedman, B.; Hodgson, K. O.; Aitken, J. B.; Levina, A.; Glover, C.; Lay, P. A. X-ray photo-chemistry and X-ray absorption spectroscopy of biological samples. *J. Synchrotron Radiat.* **2012**, *19*, 875−886.

(65) Rovezzi, M.; Lapras, C.; Manceau, A.; Glatzel, P.; Verbeni, R. High energy-resolution x-ray spectroscopy at ultra-high dilution with spherically bent crystal analyzers of 0.5 m radius. *Rev. Sci. Instrum.* **2017**, *88*, 013108.

(66) Manceau, A.; Marcus, M.; Lenoir, T. Estimating the number of pure chemical components in a mixture by X-ray absorption spectroscopy. *J. Synchrotron Radiat.* **2014**, *21*, 1140−1147.

(67) Malinowski, E. R. Theory of error for target factor-analysis with applications to mass-spectrometry and nuclear magnetic-resonance spectrometry. *Anal. Chim. Acta* **1978**, *103*, 339−354.

(68) Manceau, A.; Marcus, M. A.; Tamura, N. Quantitative speciation of heavy metals in soils and sediments by synchrotron X-ray techniques. In *Applications of Synchrotron Radiation in Low-Temperature Geochemistry and Environmental Science*; Fenter, P. A., Rivers, M. L., Sturchio, N. C., Sutton, S. R., Eds.; Mineralogical Society of America: Washington, DC, 2002; Vol. 49, pp 341−428.

(69) Thompson, D. R.; Furness, R. W. The chemical form of mercury stored in South Atlantic seabirds. *Environ. Pollut.* **1989**, *60* (3−4), 305−317.

(70) Cherel, Y.; Barbraud, C.; Lahournat, M.; Jaeger, A.; Jaquemet, S.; Wanless, R. M.; Phillips, R. A.; Thompson, D. R.; Bustamante, P. Accumulate or eliminate? Seasonal mercury dynamics in albatrosses, the most contaminated family of birds. *Environ. Pollut.* **2018**, *241*, 124−135.

(71) McCormack, M. A.; Jackson, B. P.; Dutton, J. Relationship between mercury and selenium concentrations in tissues from stranded odontocetes in the northern Gulf of Mexico. *Sci. Total Environ.* **2020**, *749*, 141350.

(72) Frodello, J. P.; Romeo, M.; Viale, D. Distribution of mercury in the organs and tissues of five toothed-whale species of the Mediterranean. *Environ. Pollut.* **2000**, *108*, 447−452.

(73) Hill, K. E.; Zhou, J. D.; McMahan, W. J.; Motley, A. K.; Atkins, J. F.; Gesteland, R. F.; Burk, R. F. Deletion of selenoprotein P alters distribution of selenium in the mouse. *J. Biol. Chem.* **2003**, *278*, 13640−13646.

(74) Nakayama, A.; Hill, K. E.; Austin, L. M.; Motley, A. K.; Burk, R. F. All regions of mouse brain are dependent on selenoprotein P for maintenance of selenium. *J. Nutr.* **2007**, *137* (3), 690−693.

(75) Ralston, N. V. C.; Raymond, L. J. Dietary selenium's protective effects against methylmercury toxicity. *Toxicology* **2010**, *278*, 112−123.

(76) Hill, K. E.; Wu, S.; Motley, A. K.; Stevenson, T. D.; Winfrey, V. P.; Capecchi, M. R.; Atkins, J. F.; Burk, R. F. Production of selenoprotein P (Sepp1) by hepatocytes is central to selenium homeostasis. *J. Biol. Chem.* **2012**, *287*, 40414−40424.

(77) Quinlivan, P. J. *Main Group and Transition Metal Complexes Supported by Carbon, Sulfur, and Selenium Donor Ligands*; Ph.D. Thesis, Columbia University, 2018.

(78) Burk, R. F.; Hill, K. E.; Olson, G. E.; Weeber, E. J.; Motley, A. K.; Winfrey, V. P.; Austin, L. M. Deletion of apolipoprotein E receptor-2 in mice lowers brain selenium and causes severe neurological dysfunction and death when a low-selenium diet is fed. *J. Neurosci.* **2007**, *27* (23), 6207−6211.

(79) Burk, R. F.; Olson, G. E.; Hill, K. E.; Winfrey, V. P.; Motley, A. K.; Kurokawa, S. Maternal-fetal transfer of selenium in the mouse. *FASEB J.* **2013**, *27* (8), 3249−3256.

(80) MacDonald, T. C.; Korbas, M.; James, A. K.; Sylvain, N. J.; Hackett, M. J.; Nehzati, S.; Krone, P. H.; George, G. N.; Pickering, I. J. Interaction of mercury and selenium in the larval stage zebrafish vertebrate model. *Metallomics* **2015**, *7* (8), 1247−1255.

(81) Earley, J. W. Description and synthesis of the selenide minerals. *Am. Mineral.* **1950**, *35*, 337−364.

(82) Pedrosa, L. F. C.; Motley, A. K.; Stevenson, T. D.; Hill, K. E.; Burk, R. F. Fecal selenium excretion is regulated by dietary selenium intake. *Biol. Trace Elem. Res.* **2012**, *149*, 377−381.

(83) Harris, H. H.; Pickering, I. J.; George, G. N. The chemical form of mercury in fish. *Science* **2003**, *301*, 1203.

(84) Bustamante, P.; Lahaye, V.; Durnez, C.; Churlaud, C.; Caurant, F. Total and organic Hg concentrations in cephalopods from the North Eastern Atlantic waters: Influence of geographical origin and feeding ecology. *Sci. Total Environ.* **2006**, *368* (2−3), 585−596.

(85) Kuwabara, J. S.; Arai, Y.; Topping, B. R.; Pickering, I. J.; George, G. N. Mercury speciation in piscivorous fish from mining-impacted reservoirs. *Environ. Sci. Technol.* **2007**, *41*, 2745−2749.

(86) Seco, J.; Xavier, J. C.; Brierley, A. S.; Bustamante, P.; Coelho, J. P.; Gregory, S.; Fielding, S.; Pardal, M. A.; Pereira, B.; Stowasser, G.; Tarling, G. A.; Pereira, E. Mercury levels in Southern Ocean squid: Variability over the last decade. *Chemosphere* **2020**, *239*, 124785.

(87) Torres-Escribano, S.; Velez, D.; Montoro, R. Mercury and methylmercury bioaccessibility in swordfish. *Food Addit. Contam., Part A* **2010**, *27* (3), 327−337.

(88) Clarkson, T. W.; Magos, L. The toxicology of mercury and its chemical compounds. *Crit. Rev. Toxicol.* **2006**, *36*, 609−662.

(89) Bridges, C. C.; Zalups, R. K. Molecular and ionic mimicry and the transport of toxic metals. *Toxicol. Appl. Pharmacol.* **2005**, *204*, 274−308.

(90) Vazquez, M.; Devesa, V.; Velez, D. Characterization of the intestinal absorption of inorganic mercury in Caco-2 cells. *Toxicol. In Vitro* **2015**, *29* (1), 93−102.

(91) Sherman, L. S.; Blum, J. D.; Franzblau, A.; Basu, N. New insight into biomarkers of human mercury exposure using naturally occurring mercury stable isotopes. *Environ. Sci. Technol.* **2013**, *47*, 3403−3409.

(92) Palmisano, F.; Cardellicchio, N.; Zambonin, P. G. Speciation of mercury in dolphin liver: A two-stage mechanism for the demethylation accumulation process and role of selenium. *Mar. Environ. Res.* **1995**, *40*, 109−121.

(93) Eagles-Smith, C. A.; Ackerman, J. T.; Yee, J.; Adelsbach, T. L. mercury demethylation in waterbird livers: dose-response thresholds and differences among species. *Environ. Toxicol. Chem.* **2009**, *28*, 568−577.

(94) Wang, Q.; Zhang, C. X.; Ren, Y. S.; Yue, W. B.; Shi, L. G.; Lei, F. L. Molecular structure, expression analysis and functional characterization of selenoprotein P (SEPP1) in goat (*Capra hircus*). *J. Anim. Vet. Adv.* **2012**, *11*, 2898−2904.

(95) Korbas, M.; O'Donoghue, J. L.; Watson, G. E.; Pickering, I. J.; Singh, S. P.; Myers, G. J.; Clarkson, T. W.; George, G. N. The chemical nature of mercury in human brain following poisoning or environmental exposure. *ACS Chem. Neurosci.* **2010**, *1*, 810−818.

(96) Labunskyy, V. M.; Hatfield, D. L.; Gladyshev, V. N. Selenoproteins: Molecular pathways and physiological roles. *Physiol. Rev.* **2014**, *94*, 739−777.

(97) Roy, A.; Kucukural, A.; Zhang, Y. I-TASSER: a unified platform for automated protein structure and function prediction. *Nat. Protoc.* **2010**, *5*, 725−738.

(98) Yang, J.; Yan, R.; Roy, A.; Xu, D.; Poisson, J.; Zhang, Y. The I-TASSER Suite: Protein structure and function prediction. *Nat. Methods* **2015**, *12*, 7−8.

(99) Zhang, S. L.; Zang, J. C.; Wang, W. M.; Chen, H.; Zhang, X. R.; Wang, F. D.; Wang, H. F.; Zhao, G. H. Conversion of the native 24-mer ferritin nanocage into its non-native 16-mer analogue by insertion of extra amino acid residues. *Angew. Chem., Int. Ed.* **2016**, *55* (52), 16064−16070.

(100) Maity, B.; Abe, S.; Ueno, T. Observation of gold sub-nanocluster nucleation within a crystalline protein cage. *Nat. Commun.* **2017**, *8*, 14820.

(101) Pozzi, C.; Ciambellotti, S.; Bernacchioni, C.; Di Pisa, F.; Mangani, S.; Turano, P. Chemistry at the protein-mineral interface in L-ferritin assists the assembly of a functional (a^3-oxo)Tris ($-^2$-peroxo) triiron(III) cluster. *Proc. Natl. Acad. Sci. U. S. A.* **2017**, *114*, 2580−2585.

(102) Hidalgo, J.; Chung, R. S.; Penkowa, M.; Vasak, M. Structure and function of vertebrate metallothioneins. *Met. Ions Life Sci.* **2009**, *5*, 279−317.

(103) Habjanic, J.; Zerbe, O.; Freisinger, E. A histidine-rich *Pseudomonas* metallothionein with a disordered tail displays higher binding capacity for cadmium than zinc. *Metallomics* **2018**, *10*, 1415−1429.

(104) Ali, M. A.; Aly, E. M.; Elawady, A. I. Effectiveness of selenium on acrylamide toxicity to retina. *Int. J. Ophthalmol.* **2014**, *7* (4), 614−620.

(105) DeLano, W. L. The PyMOL Molecular Graphics System. http://www.pymol.org, 2002.

Supporting Information for

In vivo formation of HgSe nanoparticles and Hg-tetraselenolate complex from methylmercury in seabird – Implications for the Hg-Se antagonism

Alain Manceau,*,† Anne-Claire Gaillot,‡ Pieter Glatzel,‖ Yves Cherel,§ Paco Bustamante⊥

†Univ. Grenoble Alpes, CNRS, ISTerre, 38000 Grenoble, France
‡Univ. Nantes, CNRS, Institut des Matériaux Jean Rouxel, IMN, 44000 Nantes, France
‖European Synchrotron Radiation Facility (ESRF), 71 Rue des Martyrs, 38000 Grenoble, France
§Centre d'Etudes Biologiques de Chizé (CEBC), CNRS-La Rochelle Université, 79360 Villiers-en-Bois, France.
⊥La Rochelle Université, CNRS, Littoral Environ. & Soc., LIENSs, 17000 La Rochelle, France

Number of pages: 30
Number of Tables: 3
Number of Figures: 15

Content
S1. Sample preparation
S2. Chemical analysis
S3. X-ray absorption spectroscopy
   S3.1. Measurement
   S3.2. HR-XANES analysis
   S3.3. EXAFS analysis
S4. Electron microscopy
S5. Supplementary tables
S6. Supplementary figures
S7. Supplementary references

S1. Sample preparation

During necropsies, internal tissues (liver, kidneys, pectoral muscle and brain) were sampled, weighed and wrapped individually in individual plastic bags for trace element analysis. Clotted blood was collected from heart auricles and stored in microtubes at −20 °C. Body feathers were pulled out from the lower back and stored dry in individual plastic bags. Birds were sexed during necropsies by visual gonad examination.

Prior to chemical analyses, internal tissues and blood were freeze-dried, ground to powder and then stored in plastic vials. Feathers were washed to remove surface dirt and adsorbed contaminants in a chloroform-methanol solution and then oven dried as described previously.[1] For each individual, several body feathers were pooled to limit potential inter-feather differences in Hg and Se concentrations ($n = 20$) and were homogenized by cutting them with scissors into small fragments (<1 mm).

S2. Chemical analysis

Total Hg analyses were performed with an AMA-254 mercury analyzer (Altec, Prague, Czech Republic) on dried tissue aliquots (2–4 mg) by thermal decomposition at 750 °C under oxygen flow with a detection limit of 0.05 ng Hg. All analyses were repeated 2–3 times until having a standard deviation <10%. The accuracy was controlled by analysis of a certified reference material (CRM) of lobster hepatopancreas TORT-2. The TORT-2 recommended value is 0.27 ± 0.06 µg Hg/g dw and the determined value was 0.264 ± 0.004 µg Hg/g dw ($n = 5$ measurements).

For Se, 50 to 300 mg tissue aliquots were analyzed using a Thermo Fischer Scientific X series 2 ICP-MS after digestion with 6 ml 67–70% HNO_3 and 2 ml 34–37% HCl (Fisher Scientific, trace element grade quality). Acid digestion was carried out overnight at room temperature and afterward in a Milestone microwave digestion system (30 min with a ramping temperature up to 120 °C followed by 15 min digestion at this temperature). Each sample was then completed to 50 ml with milli-Q water. Three controls (two CRM and one blank), treated and analyzed in the same way as the samples, were included in each analytical batch. CRMs were DOLT-5 dogfish liver (NRC, Canada) and TORT-3 (NRC, Canada). Analyses did not differ from the certified values with a recovery rate of 109 and 104%, respectively. The detection limit was 0.13 µg/g dry weight (dw). All Hg and Se concentrations are expressed in µg/g dw. The precision in Hg and Se concentration was assigned to 8% for all measurements.

S3. X-ray absorption spectroscopy

S.3.1. Measurement

All freeze-dried tissues of bird were pressed into 2.5 mm thick pellets, mounted in a polyether ether ketone (PEEK) sample holder sealed with Kapton tape, and maintained in a desiccator until their transfer into the liquid helium cryostat of the ID26 beamline. The storage ring was operated in the 7/8 + 1 filling mode, with 200 mA current. Rejection of higher harmonics and reduction of heat load were achieved with a white beam Pd-coated, flat mirror working under total reflection at 2.5 mrad deflecting angle. The energy of the incoming beam was selected by the 111 reflection of a Si double crystal monochromator, and the beam was focused horizontally by a second Pd-coated mirror and vertically by a third Pd-coated mirror. The flux on the sample was approximately 10^{13} photon/s in a beam footprint of ~700 (H) x 80 (V) µm² FWHM. The Hg $L_{\alpha1}$ ($3d_{5/2} \rightarrow 2p_{3/2}$) fluorescence line was selected using the 555 reflection of five spherically bent (radius = 0.5 m)[2] Si analyzer crystals (diameter = 100 mm) aligned at 81.8° Bragg angle in a vertical Rowland geometry. The diffracted intensity was measured with a Si drift diode detector

(SDD) in single photon counting mode. The effective energy resolution, obtained by convoluting the total instrument energy bandwidth (spreads of the incident and emitted rays) and the $3d_{5/2}$ core-hole width from the $L_{\alpha 1}$ line was about 3.0 eV, compared to an intrinsic line broadening of about 6.1 eV in conventional fluorescence yield measurement with a solid-state detector. Spectra were collected at a temperature of 10-15 K and a scan time of 15 s to reduce exposure, and repeated at different pristine positions on the sample to increase the signal-to-noise ratio. Scans were monitored carefully for any evidence of radiation damage. In HR-XANES mode, the incident energy was scanned from 12260 eV to 12360 eV in 0.2 eV steps and the spectra were normalized to unity at E = 12360 eV. In EXAFS mode, the incident energy was scanned from 12260 eV to 12640 eV in 2.0 eV steps. The stability in energy of the incident beam was monitored by measuring frequently a fresh MeHgCys reference. The photon energy is referenced to the maximum of the near-edge peak of MeHgCys at 12279.8 eV. The precision of the calibrated spectra is 0.1 eV.

S.3.2. HR-XANES analysis

The number of abstract components (i.e., Hg species) in the data set was evaluated in PCA with the cascade (or variance) of the eigenvalues (EVs),[3] the Malinowski's IND indicator,[4, 5] and Malinowski's F-test on reduced EVs at 5% significance level.[6, 7] The species identities were obtained subsequently by target transformation[8, 9], which makes a linear-squares fit of a reference to a weighted sum of the abstract components. The degree to which the target transformed spectrum resembles the reference being tested was evaluated with *NSS*. The lower the value, the more likely the reference is really represented in the data set. Lastly, the fractions of the Hg species in each tissue were obtained by fitting linear combinations of the single-species spectra identified by target transformation to all multicomponent spectra from the data set. The PCA and linear fit programs from beamline 10.3.2 at the Advanced Light Source were used.[9, 10]

Best-fit calculations were conducted initially with one component, then two and three components. Second and third components were retained only if their addition improved the fit quality, as evaluated from visual examination of the reconstruction and decrease of *NSS* by at least 20%. This method has been used in XANES and EXAFS studies of mercury and other elements such as zinc, iron, and thallium.[11-15] The detection threshold and accuracy of estimation of the fit components derived from the variation of *NSS* depends on the quality and complexity of the sample spectrum (i.e., number and nature of the components), the spectral characteristics of the single-species spectra (i.e., uniqueness of their features), and how well they represent the unknown sample. A generally accepted rule of thumb is that the precision on fractional amounts decreases with the number of components. There are exceptions, however, for example in a ternary system when the two major components have a similar shape and the third minor component is distinct. A prototypical case is MeHgCys which has an intense near-edge peak due to the linear coordination of Hg, whereas HgSe and $Hg(Sec)_4$ lack this feature due to the four-coordination of Hg (Figure 3). Figure S6 shows that it is possible to detect 3% MeHgCys in a mixture with HgSe and $Hg(Sec)_4$ in the kidneys of petrel P3.

S.3.3. EXAFS analysis

The EXAFS spectra were analyzed with WinXAS[16] using amplitude and phase shift functions generated by FEFF 7.0.2[17] and β-HgS[18] and HgSe[19] as structure models. The amplitude reduction factor

S_0^2 was fixed to 0.9. The accuracy of the mean bond distances R and coordination numbers (CN), including systematic errors, are within 0.02 Å and 20%, respectively (Table S3).

S4. Electron microscopy

Most STEM-HAADF images and elemental maps where acquired at 80 kV and an electron current of ~100 pA to maximize the X-ray fluorescence intensity while preserving at best the organic tissues. In contrast, the HRTEM images where acquired at 300 kV and ~6 nA to maximize the spatial resolution while keeping to phase contrast of the strong Hg and Se scatterers.

S5. Supplementary tables

Table S1. Sampling date, location, and biometrics[a] of northern giant petrels (*Macronectes halli*) from Kerguelen Islands.

Individual	Sampling date	Location	Body mass (kg)	Beak size (cm)	Tarsus size (cm)	Wing size (cm)
P1	18/09/2014	Digby	3.6	9.8	11.3	50.2
P2	12/08/2014	Ratmanov	3.4	11.3	12.2	54
P3	16/09/2014	Ratmanov	4.9	10.2	12.6	53.5
P4	06/07/2014	Pointe Rose	4.9	9.68	12.4	49
P5	29/08/2014	Anse des Papous	5.2	10.2	12	55.5

[a]The sampling location and biometrics of individuals 6 to 8 are unknown, but all were southern giant petrels (*M. giganteus*).

Table S2. Tissue mercury and selenium concentrations from chemical analysis, Hg speciation from HR-XANES spectroscopy, and bioavailable Se concentrations and elemental molar ratios used for the bar charts of Figure 1 and the graphs of Figures 2 and 6.

Petrel	Tissue	Chemical analysis				HR-XANES					Hg - bound Se^a	(Hg:Se) eff^b	(Se:Hg) eff	$[Se]_{bio}$: $[Se]_{tot}$	$[Se]_{bio}$ $\mu g/g^c$	$[Se]_{app}$ $\mu g/g^d$
		$[Hg]$ $\mu g/g$	$[Se]$ $\mu g/g$	(Hg:Se) chem	(Se:Hg) chem	f(MeHgCys)	f(Hg(Cys)$_2$)	f(HgSe)	f(Hg(Sec)$_4$)	NSS						
P1	Feathers	4.8	5.9	0.32	3.13	100 ± 5	0	0	0	6.2 10^{-5}	0.00	0.00	-	1.00	-	-
	Liver	226	175	0.51	1.97	< 3	0	100 ± 5	0 ± 4	8.4 10^{-6}	1.00	0.51	1.97	0.49	86.0	86.0
	Kidneys	54.5	151	0.14	7.04	< 3	0	62 ± 7	38 ± 7	1.8 10^{-5}	1.00	0.30	3.29	0.70	105.1	129.5
	Muscle	26.6	43.3	0.24	4.13	< 3	0	28± 8	72 ± 7	2.9 10^{-5}	0.96	0.77	1.31	0.23	10.2	32.8
	Blood	3.2	50.6	0.025	39.80	100 ± 5	0 ± 10	0	0	6.5 10^{-5}	0.00	0.00	-	1.00	50.6	49.3
P2	Feathers	26.2	11.7	0.88	1.14	100 ± 5	0	0	0	4.9 10^{-5}	0.00	0.00	-	1.00	-	-
	Liver	804	492	0.64	1.55	< 3	0	100 ± 5	0 ± 4	7.8 10^{-6}	1.00	0.64	1.55	0.36	175.5	175.5
	Kidneys	37.7	106	0.14	7.14	7 ± 3	0	61 ± 8	32 ± 9	2.2 10^{-5}	0.93	0.26	3.78	0.74	78.0	91.2
	Muscle	42.0	50.8	0.33	3.07	< 3	0	33 ± 8	67 ± 8	1.9 10^{-5}	1.00	0.98	1.02	0.02	1.0	34.3
	Blood	4.1	97.0	0.017	59.74	n.a.	n.a.	n.a.	n.a.	-	-	-	-	-	-	95.4
P3	Feathers	14.9	6.2	0.95	1.05	100 ± 5	0	0	0	5.4 10^{-5}	0.00	0.00	-	1.00	-	-
	Liver	293	213	0.54	1.85	< 3	0	91 ± 6	9 ± 6	1.5 10^{-5}	1.00	0.69	1.45	0.31	66.5	97.7
	Kidneys	40.9	122	0.13	7.58	12 ± 3	0	62 ± 7	26 ± 9	1.4 10^{-5}	0.88	0.22	4.56	0.78	95.3	105.9
	Muscle	21.8	20.9	0.41	2.44	7 ± 3	0	33 ± 9	60 ± 9	2.9 10^{-5}	0.93	1.12	0.89	-0.12	-2.5	12.3
	Blood	8.7	102	0.034	29.78	88 ± 8	12 ± 9	0	0	6.4 10^{-5}	0.00	0.00	-	1.00	102.0	98.6
P4	Feathers	12.3	9.9	0.49	2.04	100 ± 5	0	0	0	5.4 10^{-5}	0.00	0.00	-	1.00	-	-
	Liver	1499	1101	0.54	1.87	< 3	0	90 ± 6	10 ± 6	1.1 10^{-5}	1.00	0.70	1.42	0.30	328.0	510.9
	Kidneys	414	363	0.45	2.23	< 3	0	71 ± 7	29 ± 7	1.9 10^{-5}	1.00	0.84	1.19	0.16	58.3	200.0
	Muscle	88.7	72.7	0.48	2.08	< 3	0	60 ± 8	40 ± 8	2.2 10^{-5}	1.00	1.06	0.95	-0.06	-4.1	37.8
	Blood	4.7	81.9	0.023	44.39	n.a.	n.a.	n.a.	n.a.	-	-	-	-	-	-	80.1
P5	Feathers	10.3	7.8	0.52	1.92	100 ± 5	0	0	0	6.4 10^{-5}	0.00	0.00	-	1.00	-	-
	Liver	170	109	0.61	1.63	< 3	0	94 ± 6	6 ± 6	1.3 10^{-5}	1.00	0.72	1.38	0.28	30.0	42.1
	Kidneys	9.8	55	0.07	14.20	< 3	0	48 ± 9	52 ± 9	3.5 10^{-5}	1.00	0.18	5.55	0.82	45.1	51.1
	Muscle	2.9	10.1	0.11	8.96	11 ± 5	0	22 ± 11	67 ± 13	5.0 10^{-5}	0.89	0.32	3.09	0.68	6.8	9.0
	Blood	1.3	43.4	0.011	87.50	61 ± 7	39 ± 8	0	0	5.9 10^{-5}	0.00	0.00	-	1.00	43.4	42.9
P6	Feathers	8.5	24.2	0.14	7.23	n.a.	n.a.	n.a.	n.a.	-	-	-	-	-	-	-

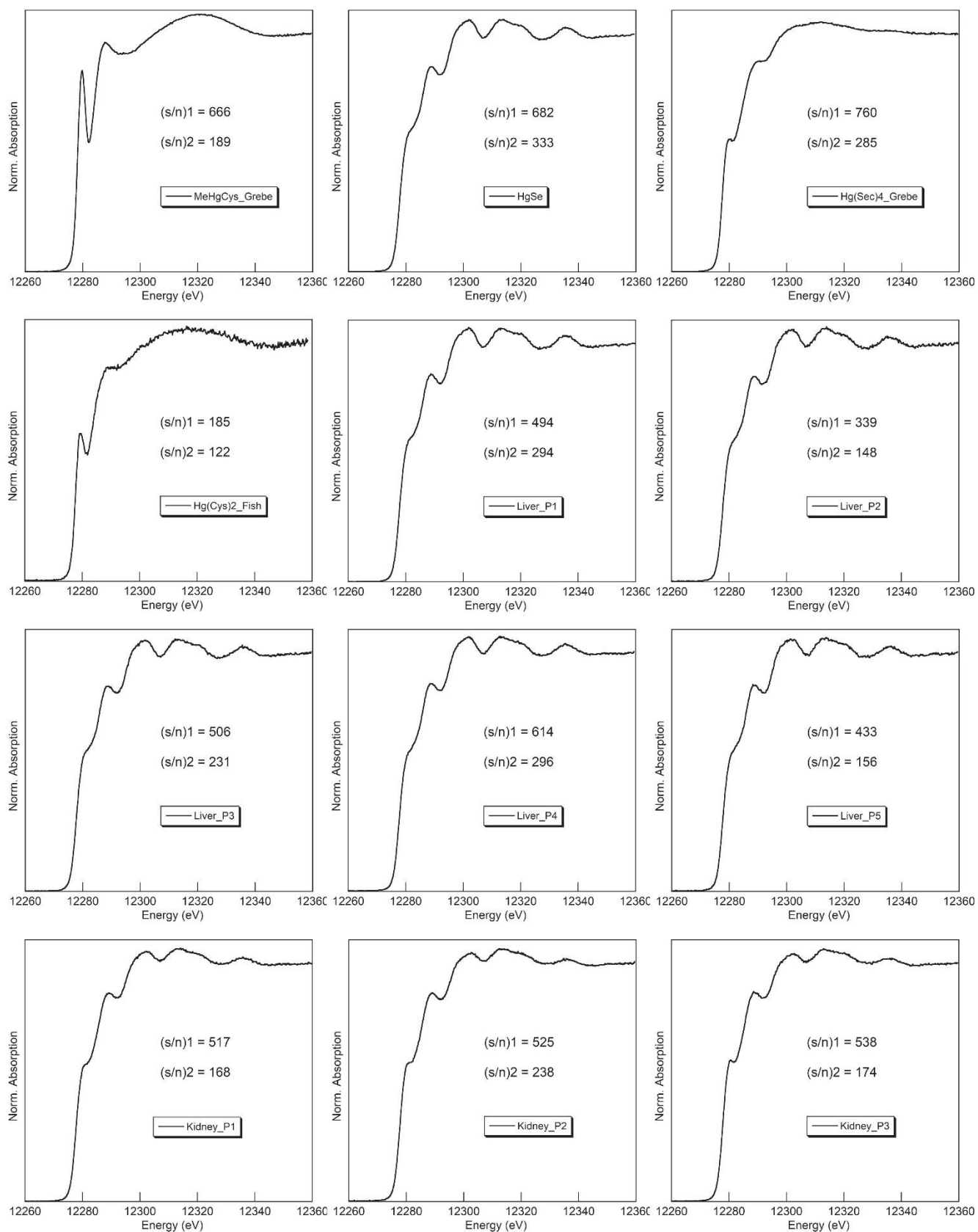| Group	Tissue															
	Liver	214	113	0.74	1.35	n.a.	n.a.	n.a.	n.a.	-	-	-	-	-	-	29.2
	Kidneys	27.5	159	0.068	14.70	n.a.	n.a.	n.a.	n.a.	-	-	-	-	-	-	148.5
	Muscle	4.2	31.7	0.052	19.36	n.a.	n.a.	n.a.	n.a.	-	-	-	-	-	-	30.1
	Brain	2.8	43.1	0.026	38.55	40 ± 6	0	36 ± 13	24 ± 15	$4.9\,10^{-5}$	0.60	0.03	29.21	0.97	41.6	42.0
	Blood	3.0	118	0.010	101.02	n.a.	n.a.	n.a.	n.a.	-	-	-	-	-	-	116.9
P7	Feathers	10.3	14.0	0.29	3.45	n.a.	n.a.	n.a.	n.a.	-	-	-	-	-	-	-
	Liver	n.a.	n.a.	-	-	n.a.	n.a.	n.a.	n.a.	-	-	-	-	-	-	n.a.
	Kidneys	39.9	87.1	0.18	5.55	n.a.	n.a.	n.a.	n.a.	-	-	-	-	-	-	71.4
	Muscle	1.7	15.1	0.043	23.11	n.a.	n.a.	n.a.	n.a.	-	-	-	-	-	-	14.4
	Brain	1.6	26.2	0.024	42.09	83 ± 5	0	8 ± 8	9 ± 9	$4.9\,10^{-5}$	0.17	0.01	95.67	0.99	25.9	25.6
	Blood	3.0	68.5	0.017	57.43	n.a.	n.a.	n.a.	n.a.	-	-	-	-	-	-	67.3
P8	Feathers	21.2	8.6	0.97	1.03	n.a.	n.a.	n.a.	n.a.	-	-	-	-	-	-	-
	Liver	405	191	0.83	1.20	n.a.	n.a.	n.a.	n.a.	-	-	-	-	-	-	32.0
	Kidneys	50.8	134	0.15	6.67	n.a.	n.a.	n.a.	n.a.	-	-	-	-	-	-	113.5
	Muscle	29.2	35.1	0.33	3.06	n.a.	n.a.	n.a.	n.a.	-	-	-	-	-	-	23.6
	Brain	13.2	47.0	0.11	9.05	13 ± 5	0	71 ± 8	16 ± 10	$2.0\,10^{-5}$	0.87	0.15	6.70	0.85	40.0	41.8
	Blood	23.9	96.6	0.10	10.26	n.a.	n.a.	n.a.	n.a.	-	-	-	-	-	-	87.2

n.a.: not available. [a]Atomic fraction. [b]Effective atomic ratio. [c]Concentration of bioavailable Se. [d]Apparent concentration of bioavailable Se.
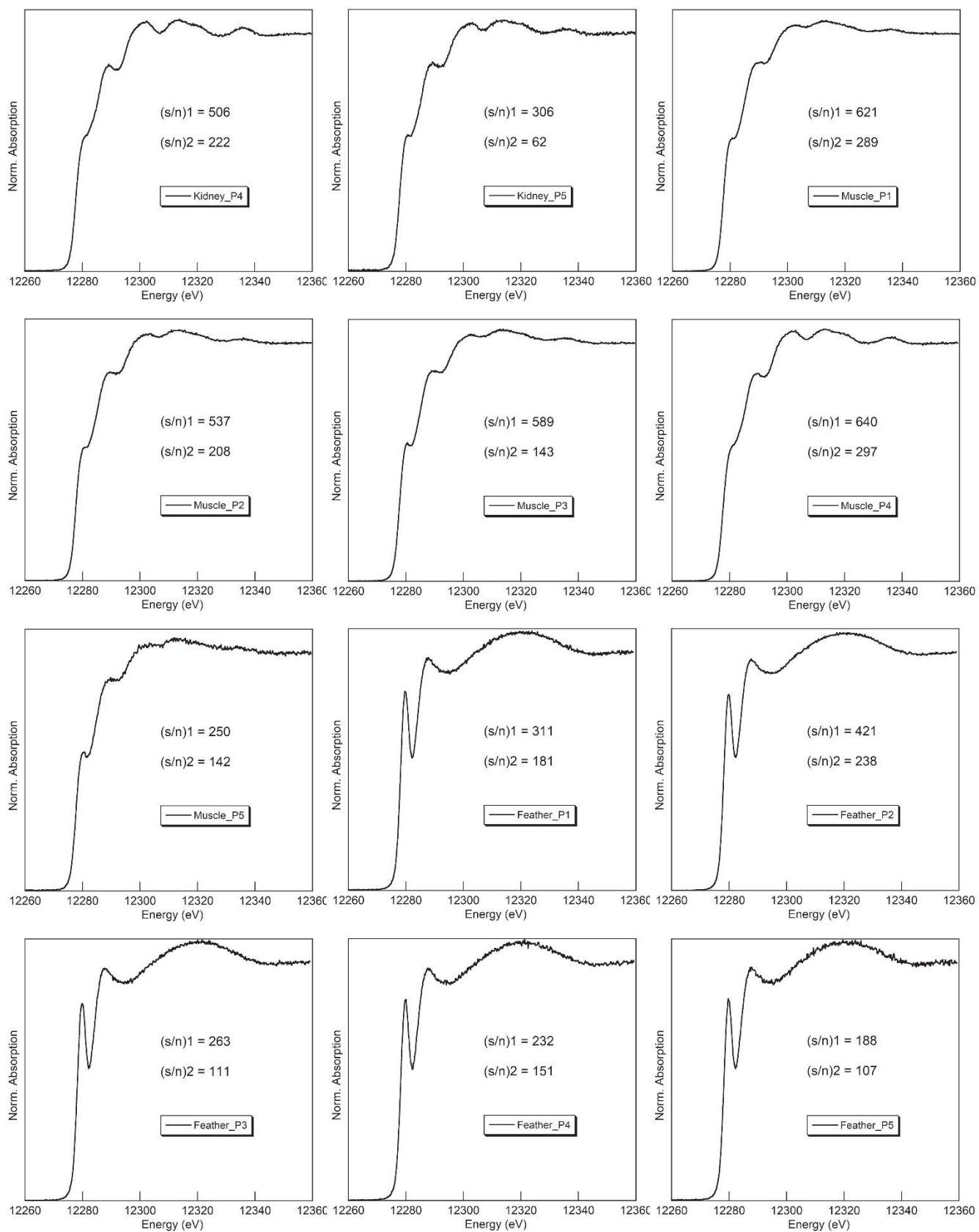
Table S3. Structural parameters derived from the EXAFS analysis of the liver tissue for petrel P2

	Hg-Se$_1$			Hg-Hg$_1$			Hg-Se$_2$		
CN	*R* (Å)	σ^2 (Å^2)	*CN*	*R* (Å)	σ^2 (Å^2)	*CN*	*R* (Å)	σ^2 (Å^2)	ΔE (eV)[a]
4[b]	2.64	0.003	12[b]	4.35	0.016[c]	12[b]	5.08	0.016[c]	5.1

[a]Shift of the energy threshold. [b]Coordination numbers fixed to crystallographic values.[19] [c]Parameters constrained identical. Fit residual *Res* = [$\Sigma\{|\chi_{exp} - \chi_{fit}|\}/\Sigma\{|\chi_{exp}|\}$] x 100 = 4.7.

S6. Supplementary figures

(s/n)1 = 506
(s/n)2 = 222
Kidney_P4

(s/n)1 = 306
(s/n)2 = 62
Kidney_P5

(s/n)1 = 621
(s/n)2 = 289
Muscle_P1

(s/n)1 = 537
(s/n)2 = 208
Muscle_P2

(s/n)1 = 589
(s/n)2 = 143
Muscle_P3

(s/n)1 = 640
(s/n)2 = 297
Muscle_P4

(s/n)1 = 250
(s/n)2 = 142
Muscle_P5

(s/n)1 = 311
(s/n)2 = 181
Feather_P1

(s/n)1 = 421
(s/n)2 = 238
Feather_P2

(s/n)1 = 263
(s/n)2 = 111
Feather_P3

(s/n)1 = 232
(s/n)2 = 151
Feather_P4

(s/n)1 = 188
(s/n)2 = 107
Feather_P5

S9
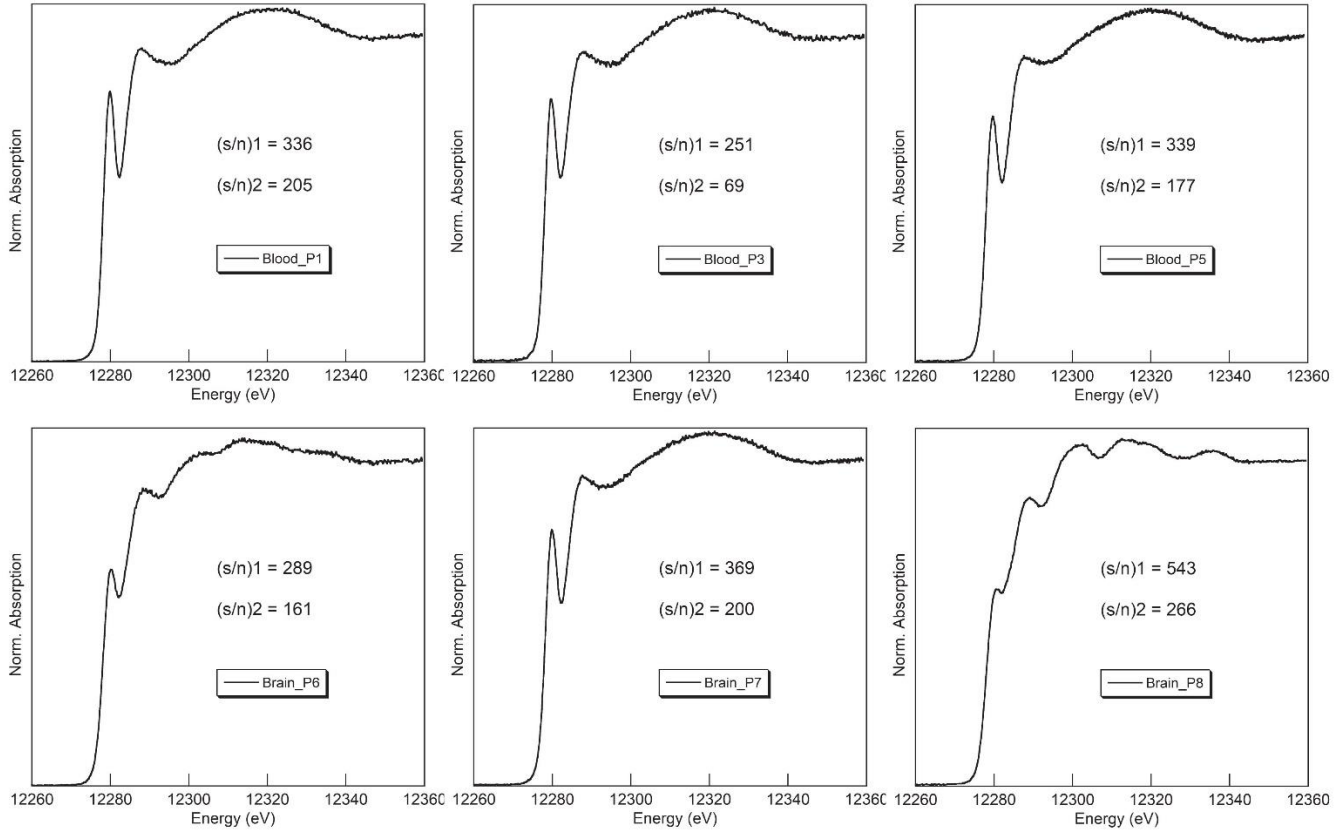
Figure S1. Plot of the 26 Hg L_3-edge HR-XANES spectra measured for this study with their signal-to-noise ratio (s/n) measured with the two following expressions[20]:

$$(s/n)_1 = \sqrt{\frac{\langle S^2 \rangle}{\mathrm{Var}(S-F)}}$$

$$(s/n)_2 = \sqrt{\frac{\langle S \rangle}{\mathrm{Var}((S-F)/\sqrt{S})}}$$

where S and F are the original signal and filtered (i.e., de-noised) data, respectively, $\langle \cdots \rangle$ is a mean over the energy range, and $\mathrm{Var}(x)$ is the variance of x sampled over the energy range. The de-noising algorithm is detailed in ref.[20].
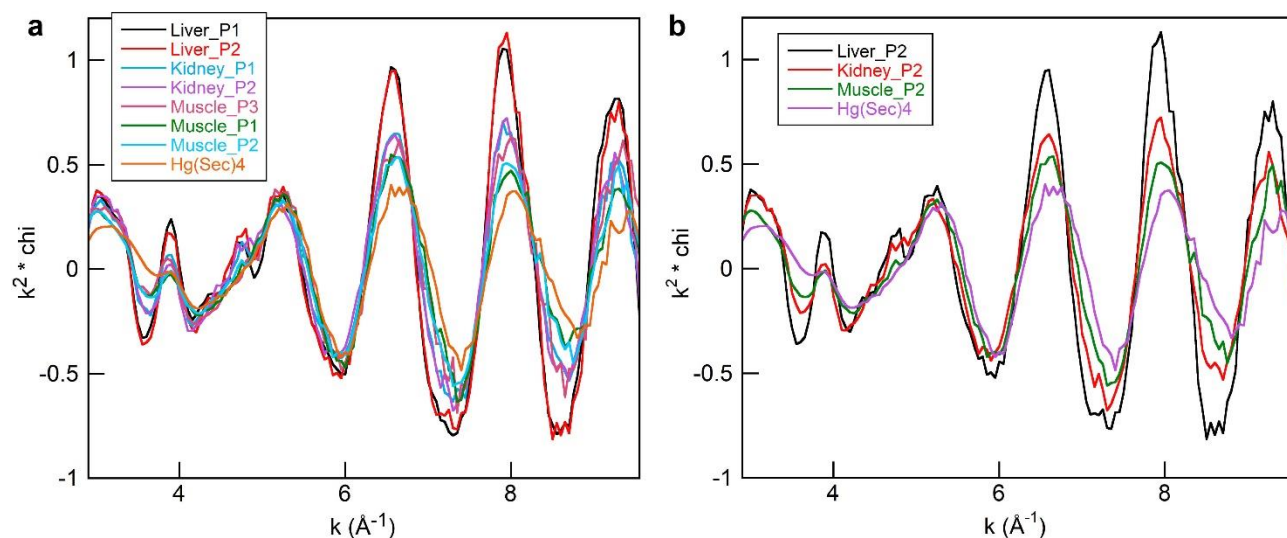
Figure S2. Mercury L$_3$-edge EXAFS spectra of giant petrel tissues (a) and the tissues from bird P2 only (b) with the spectrum from Hg(Sec)$_4$.[21] The EXAFS spectra of the kidneys and muscles are intermediate between those of the livers (100% HgSe) and Hg(Sec)$_4$, indicating that they contain variable ratios of HgSe and Hg(Sec)$_4$.
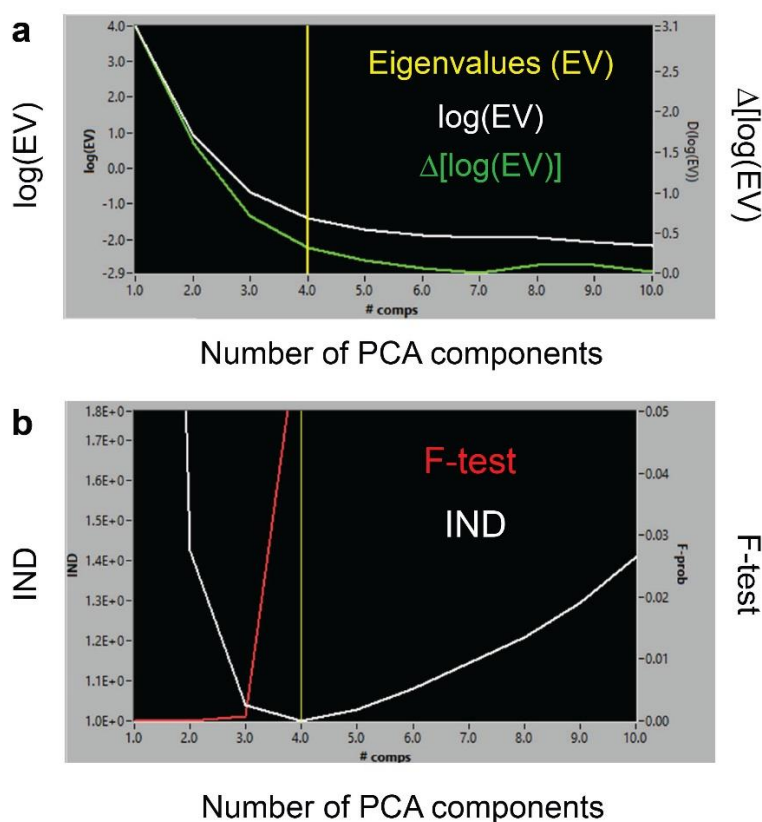
Figure S3. Estimation by PCA of the number of significant abstract components contained in the 26 HR-XANES data set from three estimators. a) Scree plot of the components and the associated eigenvalues (EVs)[3]. b) Malinowski's IND indicator[4, 5] and Malinowski's F-test at 5% significance level.[6, 7] See ref.[20] for details.
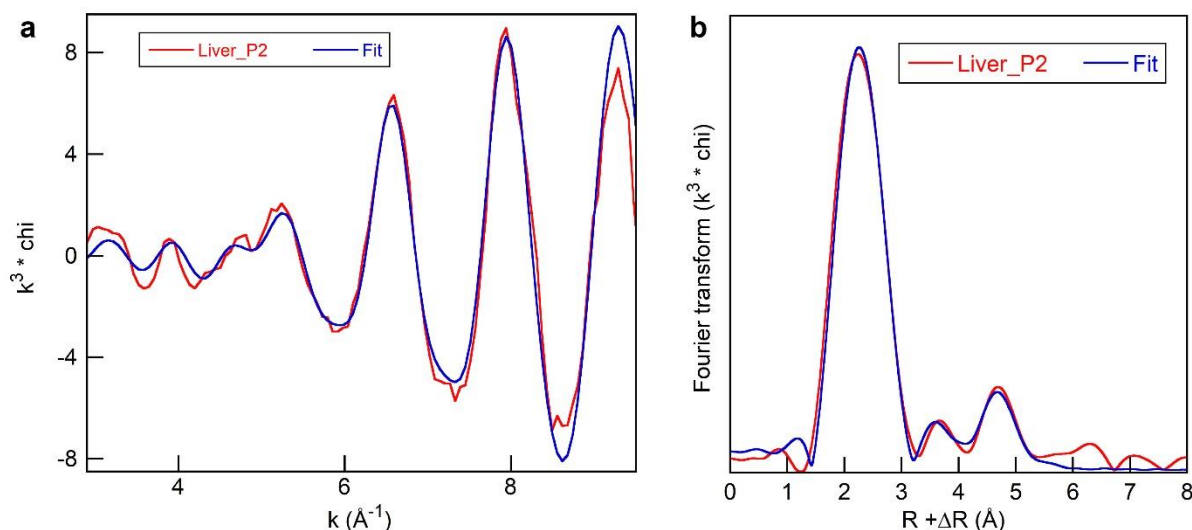
Figure S4. Fit of the EXAFS spectrum (a) and Fourier transform (b) of the liver for petrel P2. The EXAFS parameters are given in Table S3. The Hg-Se$_1$ = 2.64 Å, Hg-Hg$_1$ = 4.35 Å, and Hg-Se$_2$ = 5.08 Å distances are close to the crystallographic values of 2.63 Å, 4.30 Å, and 5.04 Å for HgSe.[19] However, the Debye-Waller term σ of the Hg-Hg$_1$ and Hg-Se$_2$ pairs, which is the mean-square displacement of the Hg-Hg$_1$ and Hg-Se$_2$ distances, is extremely large (σ^2 = 0.016 Å^2). The interatomic distances, although close on average to those in HgSe, are widely distributed, which means that the nanocrystals are highly defective, as usually observed in nanoparticles with a high surface/volume ratio.[22] The Hg atoms at their surface have a lower coordination and higher static disorder. Inclusion of sulfur atoms in the first atomic shell around the Hg atoms (Hg-(S,Se)$_1$ solid-solution) yielded a negative coordination number (CN(S) = -0.3 and CN(Se) = 4.3), indicating that the HgSe grains do not contain sulfur.
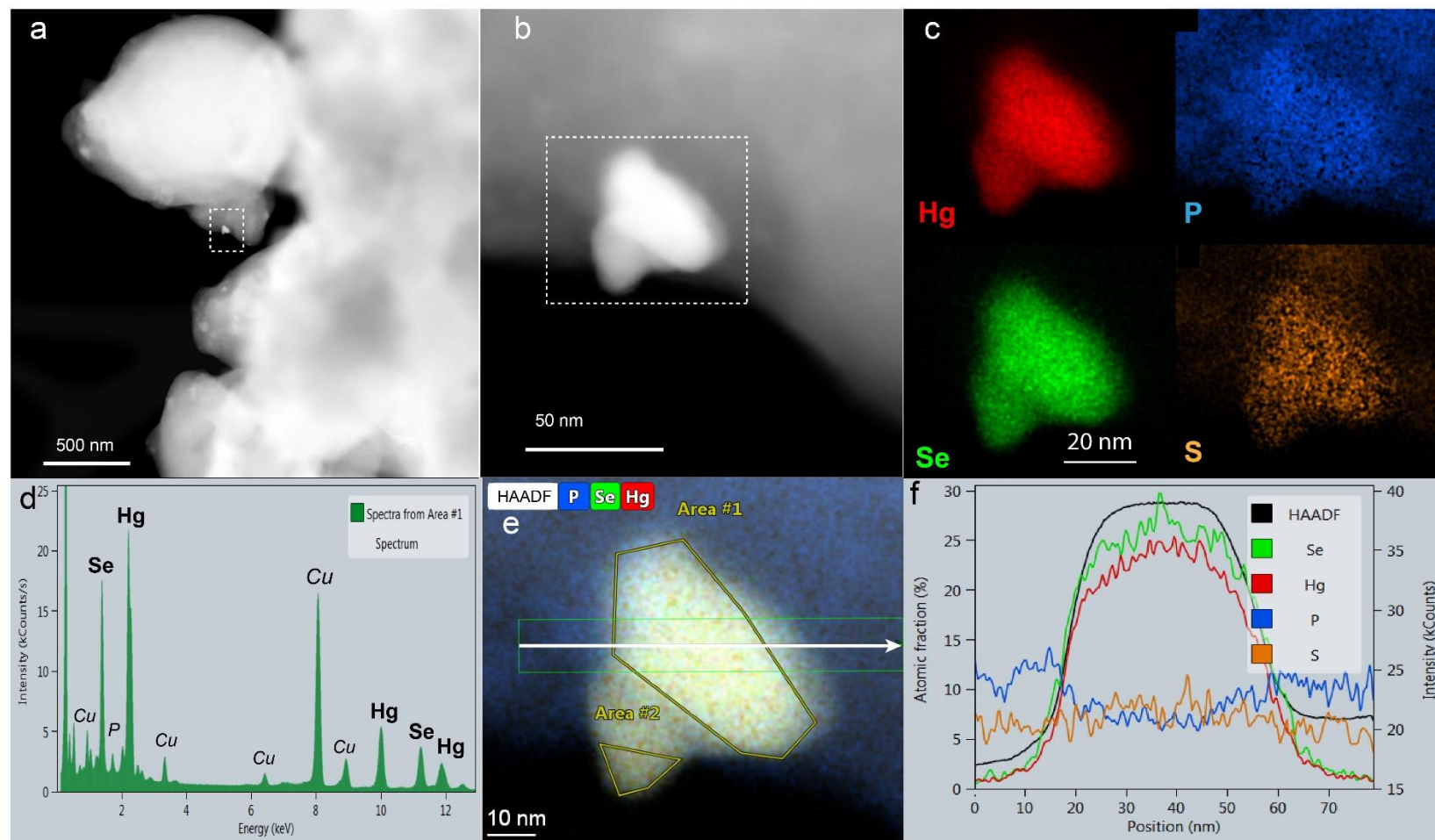
Figure S5. a-b) Low and high magnification STEM-HAADF images of the two large HgSe grains of petrel P4 shown in Figure 5a. The bright contrast in (b) comes from the large scattering power of Hg and Se. c) EDX maps of Hg (red), Se (green), P (blue), and S (orange). d) Summed EDX spectrum from the point spectra of the larger grain (framed area #1 in (e)). C, O, P, K, and Fe fluorescence lines are from the organic tissue and the Cu line from the copper grid. They are not seen in the summed spectrum from the smaller grain sticking out from the tissue (area #2 – not shown). e) Superimposition of the HAADF image and P, Se and Hg maps. The white arrow across the larger grain indicates the position and direction of the concentration profiles shown in (f). f) Post-acquisition EDX line profiles (~30 pixels wide = green box in (e)) across the larger grain expressed in atomic fraction (%) of Se (green), Hg (red), P (blue), and S (orange). The black profile is the scattering contrast of the HAADF image (expressed in kcounts).
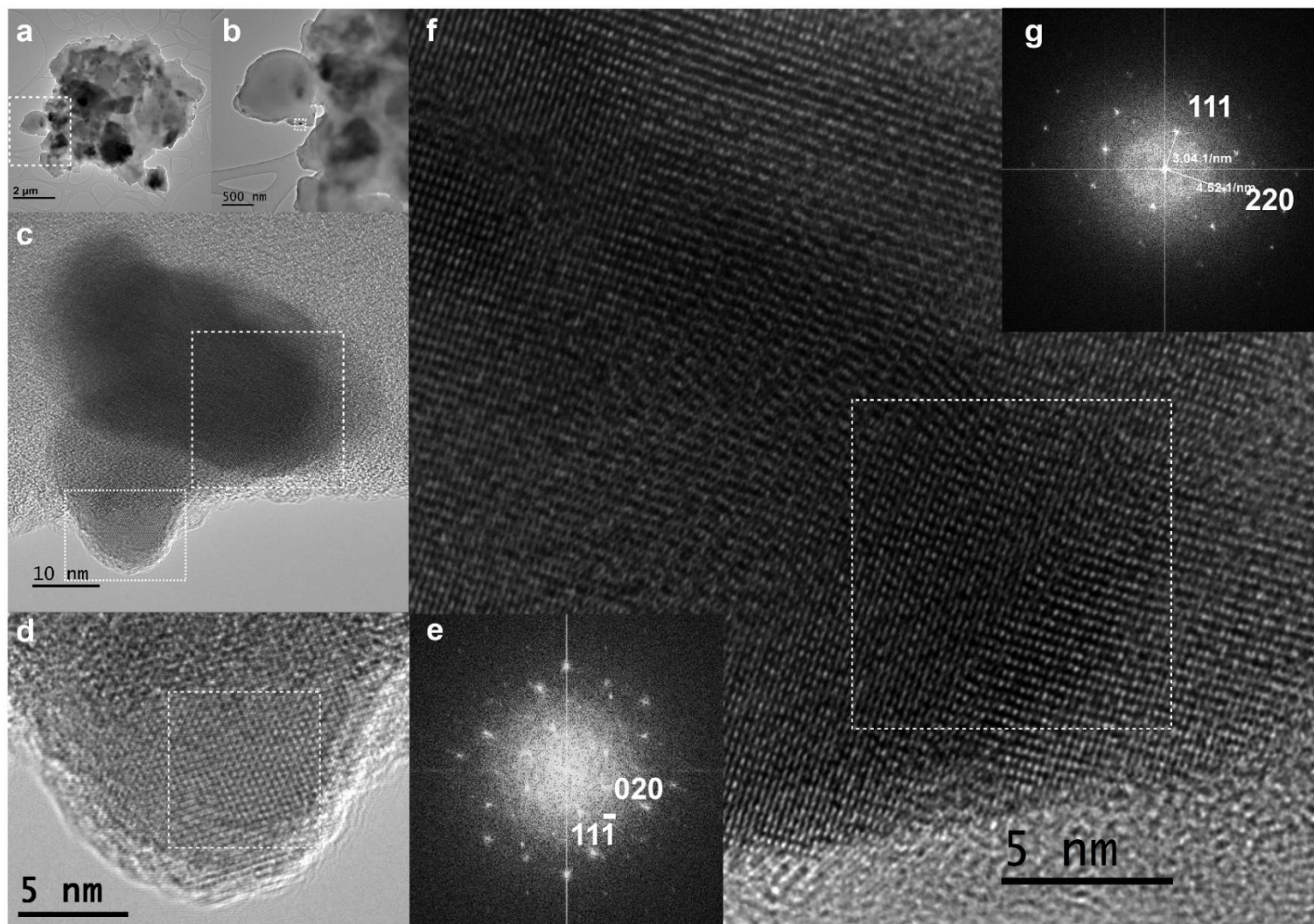
Figure S6. a-c) HRTEM images of the same zone shown in Figure S5, demonstrating the crystallinity of the precipitates. Heavy elements (and thicker areas) appear as dark contrast. c) HRTEM image of the two $HgSe_{NP}$ located in the rectangular region of (a). d,f) Magnification of the framed area of the smaller (d) and larger (f) HgSe grain in (c). e,g) FFT patterns of the boxed areas in (d) and (f). The patterns correspond to the [101] (e) and [112] (g) zone axes of HgSe (space group $Fd3m$) with $a = 6.08$ Å.
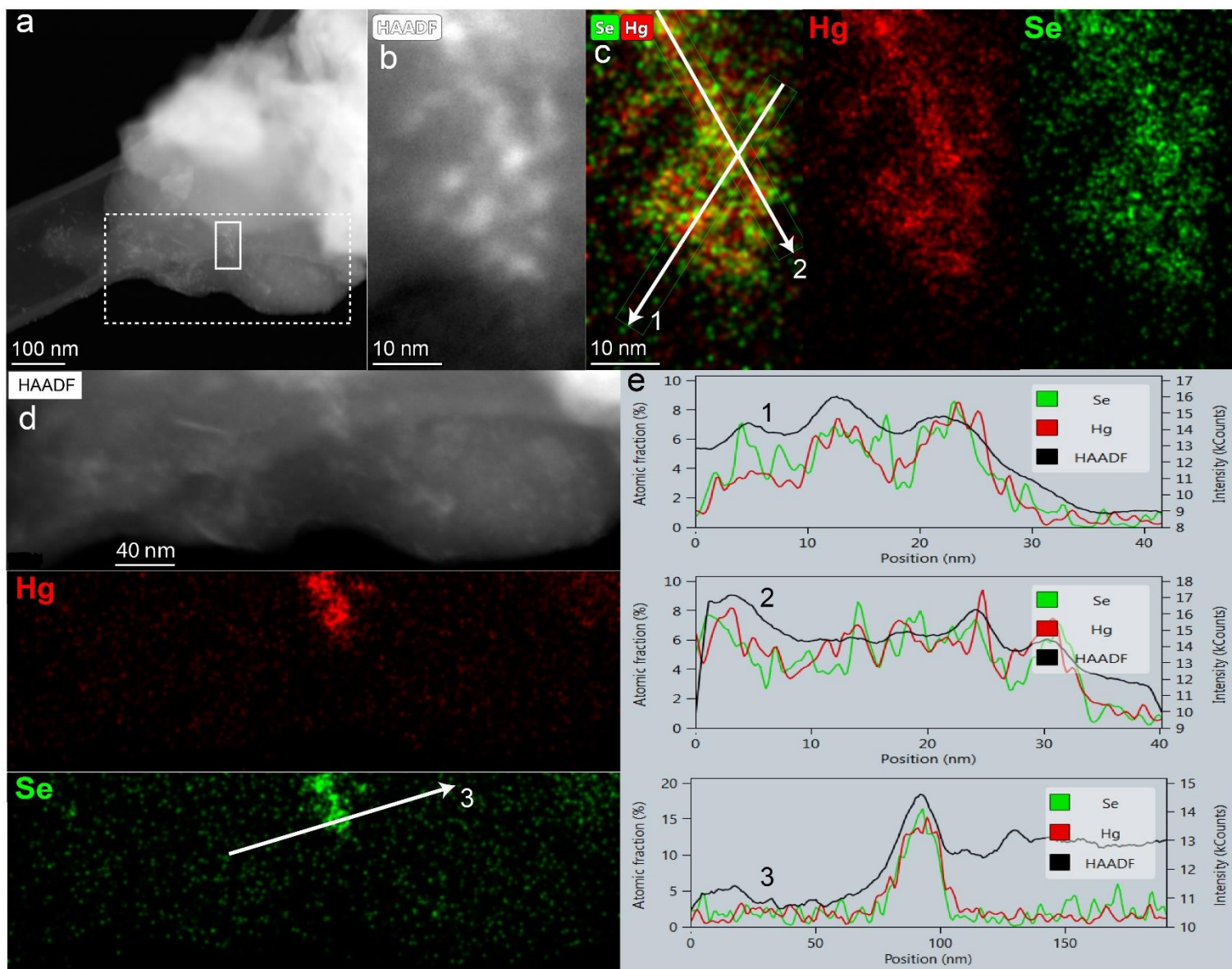
Figure S7. a) STEM-HAADF image of a liver region of petrel P4 rich in HgSe_{NP} aggregates. b) Magnification of the (a) area framed with a plain line. c) EDX maps in fluorescence counts of Hg (red) and Se (green), and Hg-Se bi-color map of the (b) region. The arrows indicate the positions and directions of the EDX line profiles 1 and 2 shown in (e). d) Magnification of the (a) area framed with a dashed line (top), and

Hg and Se EDX maps (bottom). The arrow indicates the position and direction of the EDX transect 3, which extends on both sides of the aggregate. e) Post-acquisition EDX line profiles (~30 pixels wide) of Hg (red) and Se (green) expressed in atomic fraction (%), and scattering contrast of the HAADF image (black, in kcounts). Transect 3 shows that the area surrounding the HgSe$_{NP}$ aggregate is not enriched in selenium (e.g., SelP protein). The Se:Hg ratio is statistically equal to 1.
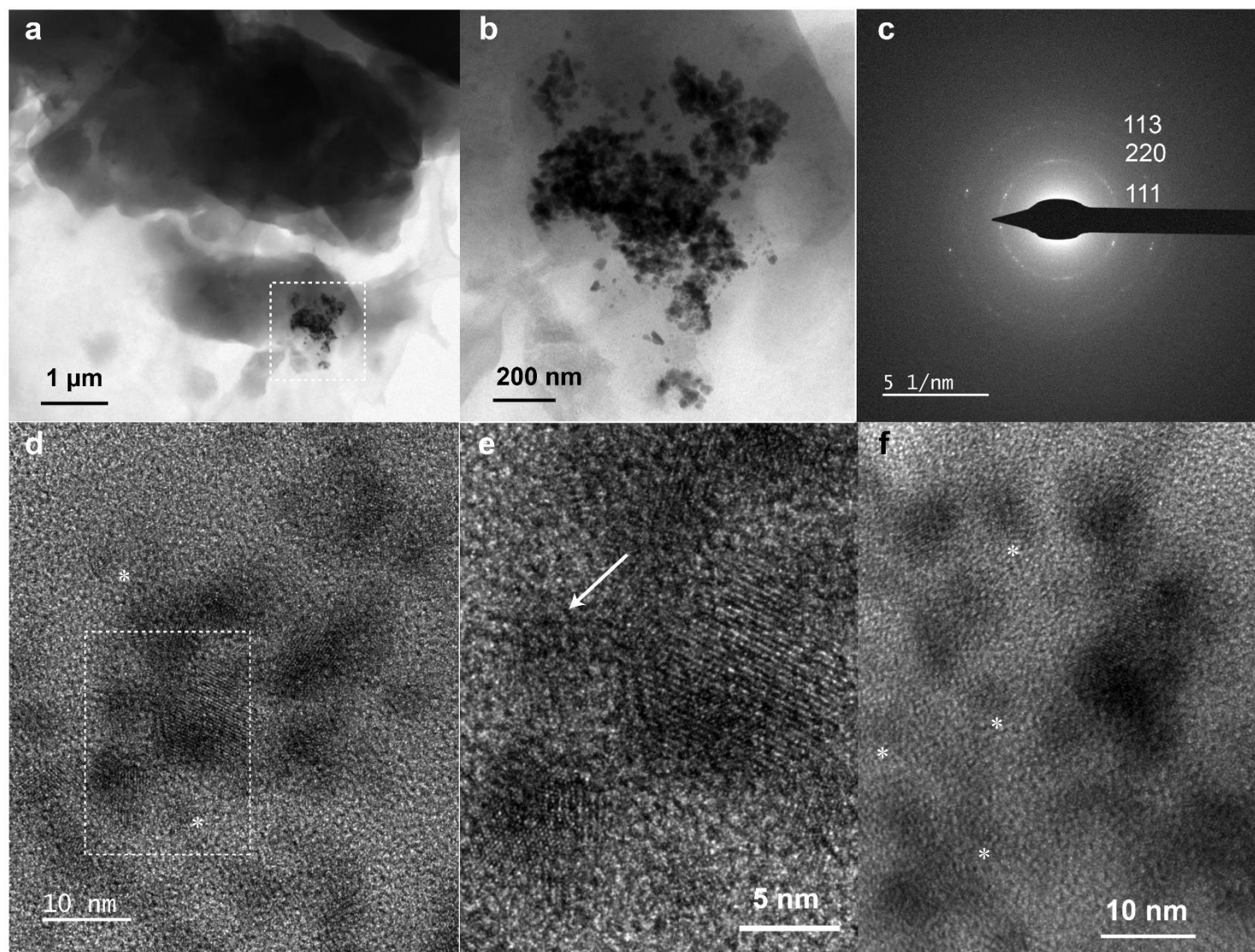
Figure S8. a) TEM image of pieces of dried kidney tissue of petrel P4. b) Zoom of a highly contrasted micron-size aggregate of HgSe$_{NP}$ corresponding to the boxed area in (a). c) Selected-area electron diffraction (SAED) pattern of the whole aggregate in (b). The first rings match up with the 111, 220, and 113 diffraction lines of the *Fd*3*m* cubic structure of HgSe with $a = 6.08$ Å. d-f) HRTEM images of isolated HgSe$_{NP}$ crystals. Star symbols point out less than 3 nm nanoparticules, barely distinguishable on the C-coated membrane (and potentially some organic matter) of the TEM grid support. e) Zoom of the boxed area in (d) showing the hexagonal phase-contrast pattern compatible with the common {111} orientation of the cubic structure of NP. The arrow points out a less than 3 nm NP.
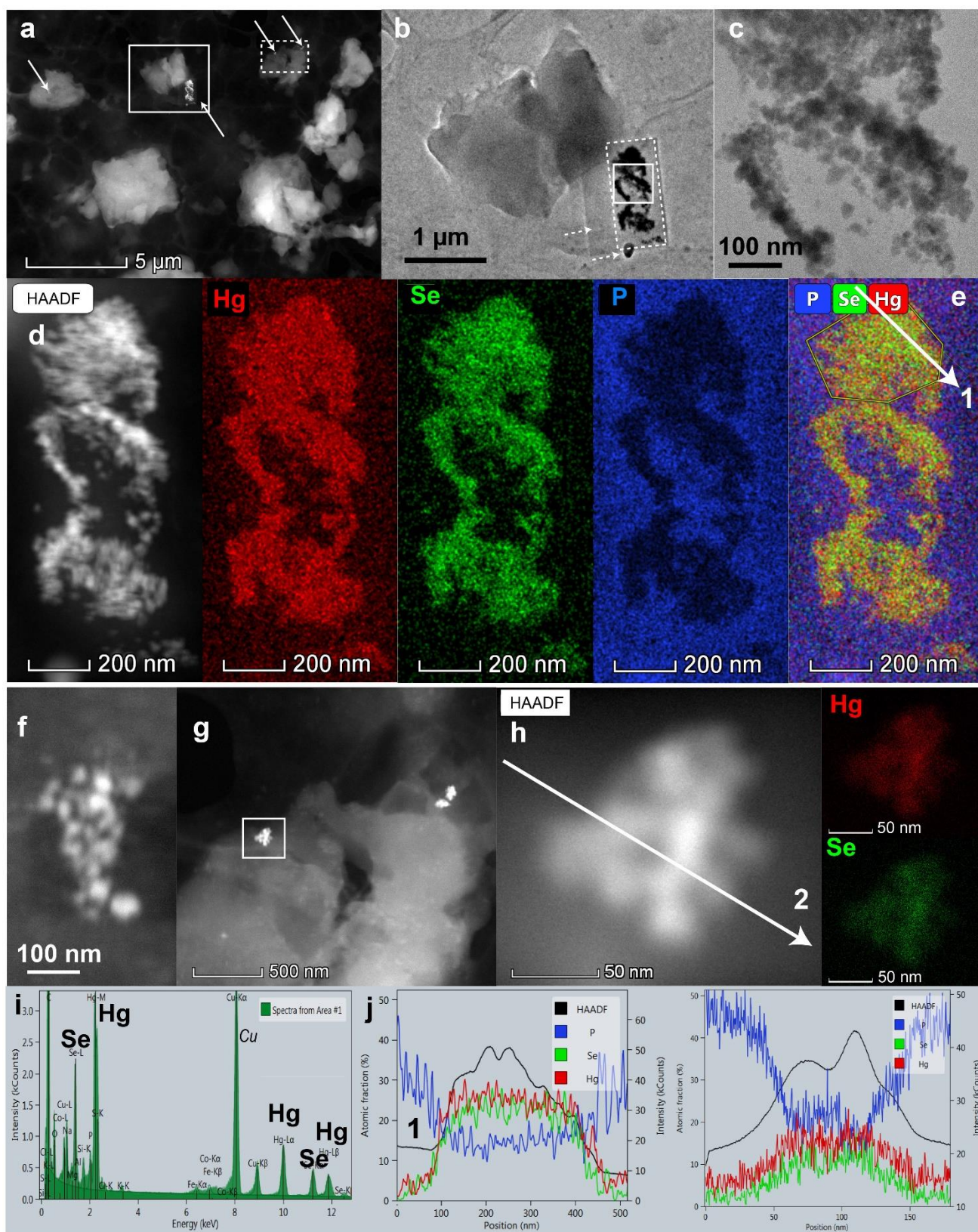
Figure S9. a) STEM-HAADF image of several pieces of dried kidney tissue of petrel P4 containing HgSe$_{NP}$ aggregates of various sizes pointed out with arrows. b) TEM image of the piece framed with a plain line in (a). The aggregate is >1 µm in length. c) Magnification of the framed area in (b) showing

HgSe$_{NP}$ of different sizes ranging from 5 to 30 nm. d) HAADF image of the large HgSe$_{NP}$ aggregate framed in the dotted box in (b), and EDX maps of Hg (red), Se (green), and P (bleu) in atomic fraction. e) Hg-Se-P tri-color map (in atomic fraction) showing the distinct location of P from Hg and Se. The white arrow indicates the position and direction of the EDX line profile 1 (30 pixels wide) shown in (j). (f) HAADF image of the HgSe$_{NP}$ aggregate pointed out with the arrow on the upper left of (a). (g) HAADF image of the area framed with a dotted line on the upper right of (a). h) Magnification of the framed area in (g) and EDX maps in fluorescence counts of Hg (red) and Se (green). The white arrow indicates the position and direction of the EDX line profile 2 (30 pixels wide) shown in (j). i) Summed EDX spectrum from the area framed in yellow in the upper part of image (e). j) Post-acquisition EDX line profiles 1 and 2 of Hg (red), Se (green), and P (blue) in atomic fraction (%), with the HAADF contrast (black – in kcounts), showing that the HgSe$_{NP}$ grains are stoichiometric and that P belongs to the surrounding tissue.
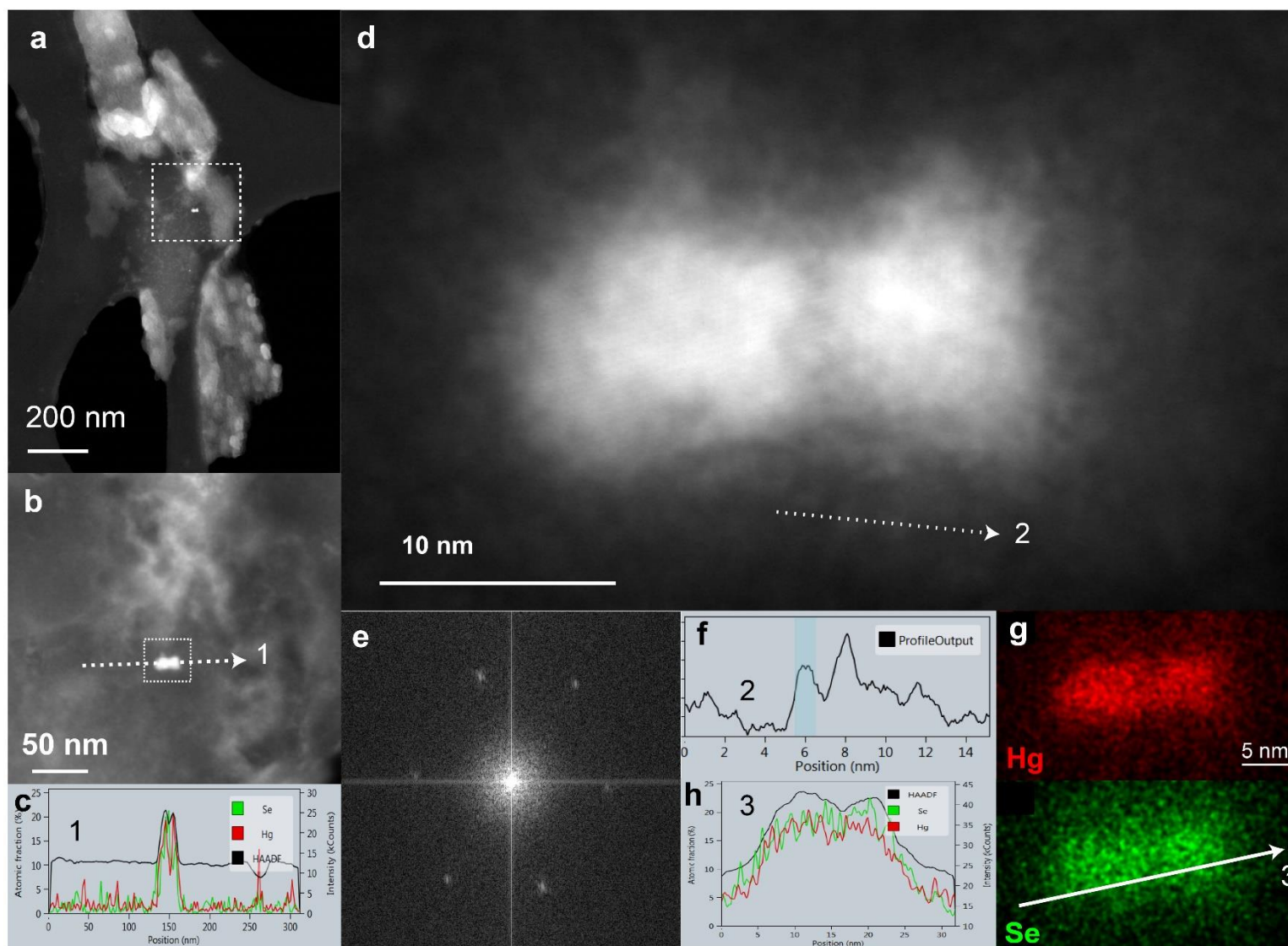
Figure S10. a) STEM-HAADF image of a piece of dried kidney tissue of petrel P4. (b) Magnification of the framed area in (a) showing several HgSe$_{NP}$ aggregates. The white arrow indicates the position and direction of the EDX line profile 1 (30 pixels wide) displayed in (c). c) Post-acquisition EDX line profile 1 of the atomic fraction (%) of Hg (red) and Se (green), with HAADF contrast (black, in kcounts), confirming the HgSe composition of the grains and the absence of Hg and Se in the vicinity of the grains. The spikes are from pixels with low statistic of

X-ray counts in the absence of matter. d) STEM-HAADF image of the two 5 nm aggregates from the framed area in (b) with FFT in (e), demonstrating their crystalline nature. The white arrow indicates the position and direction of the HAADF intensity profile 2 in (f). (f) Intensity profile 2 along a 14 nm long line measured below the twinned aggregates showing that the aggregates consist of a mosaic of ~1 nm nanograins. The nanograins in the twinned aggregates are structurally coherently oriented, as demonstrated by the FFT (e). g) EDX maps of Hg (red) and Se (green) of the two HgSe twinned aggregates imaged in (b) and (d). The white arrow indicates the position of the EDX line profile 3 displayed in (h). (h) Post-acquisition EDX line profile 3 of the atomic fraction (%) of Hg (red) and Se (green), with HAADF contrast (black).
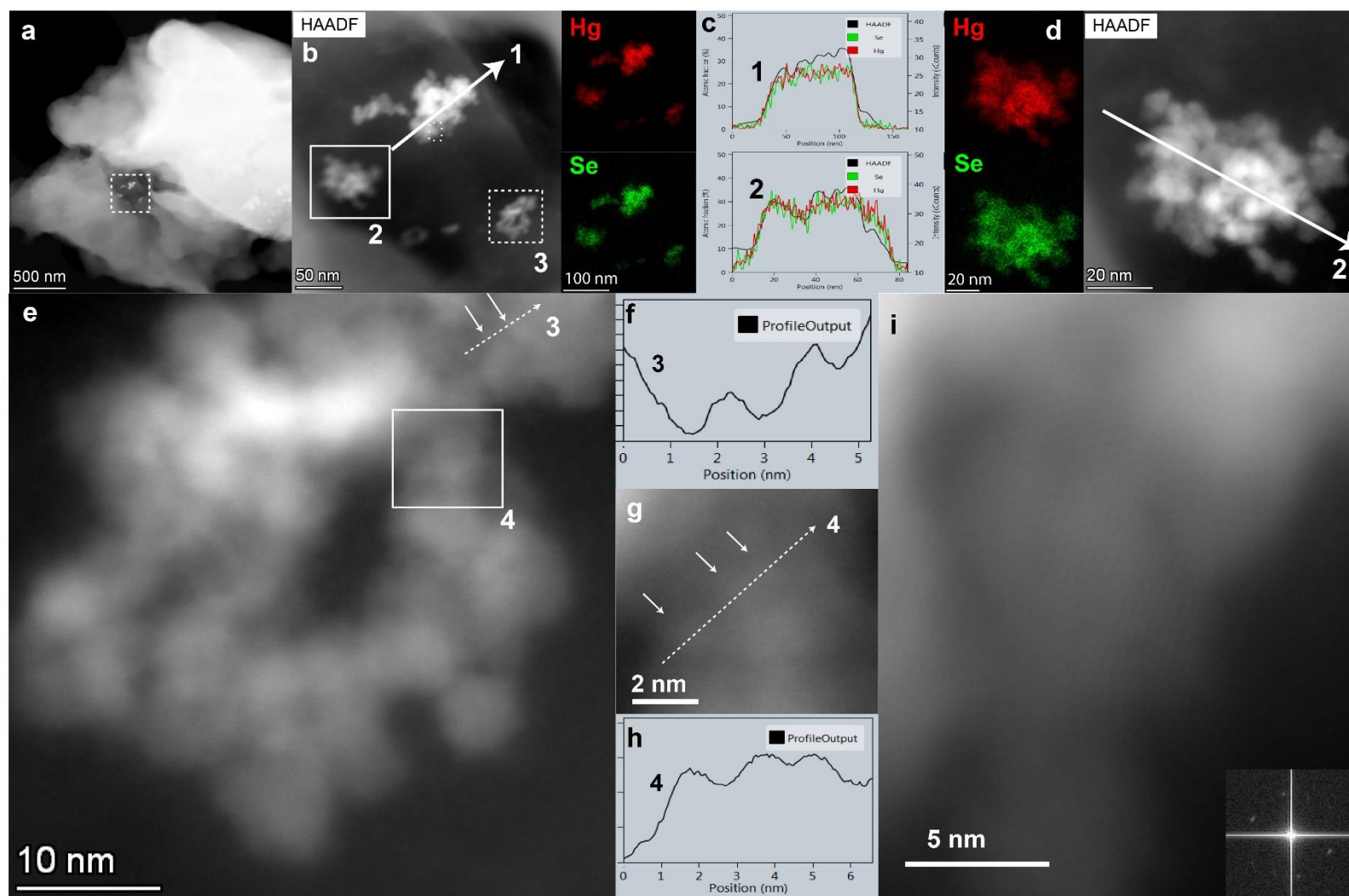
Figure S11. a) STEM-HAADF image of dried kidney tissue of petrel P4. b) Zoom on several aggregates of HgSe_NP of various sizes ranging from 5 nm (isolated NP) to 100 nm, and corresponding EDX maps of Hg (red) and Se (green). The arrow indicates the position and direction of the EDX intensity profile 1 (30 pixels wide) displayed in (c). The areas framed with plain, dashed and dotted lines are zoomed in (d), (e), and (i), respectively. c)12 pm Post-acquisition EDX line profiles 1 and 2 of Hg (red) and Se (green) in atomic fraction (%), with the HAADF contrast (black, in kcounts), showing that the HgSe_NP grains are stoichiometric throughout the aggregates. d) STEM-HAADF image of the

bottom-left HgSe$_{NP}$ aggregate 2 framed with plain line in (b), and corresponding EDX maps of Hg (red) and Se (green). The arrow indicates the position and direction of the EDX intensity profile 2 (30 pixels wide) shown in (c). e) HR-STEM-HAADF image of the bottom-right HgSe aggregate 3 framed with a dashed line in (b). The two plain arrows point out less than 1 or 2 nm size HgSe$_{NP}$ as estimated from the intensity profile shown in (f). The embedding organic tissue hinders the quality of the image and a better estimate of the NP diameter. f) Intensity profile 3 along the direction shown by the dotted arrow 3 across the NPs in the upper right of (e). g) Zoomed image of the framed area in (e) showing 1-2 nm size NPs pointed out by plain arrows. h) Intensity profile 4 along the direction shown by the dotted arrow 4 across the NPs in (g). i) HR-STEM-HAADF image of the framed area with dotted line from aggregate 1 in (b), and FFT of the central nanograin. The FFT is consistent with the $Fd3m$ cubic structure of HgSe with $a = 6.08$ Å and a [101] zone-axis orientation, as in Fig. S6d,e.
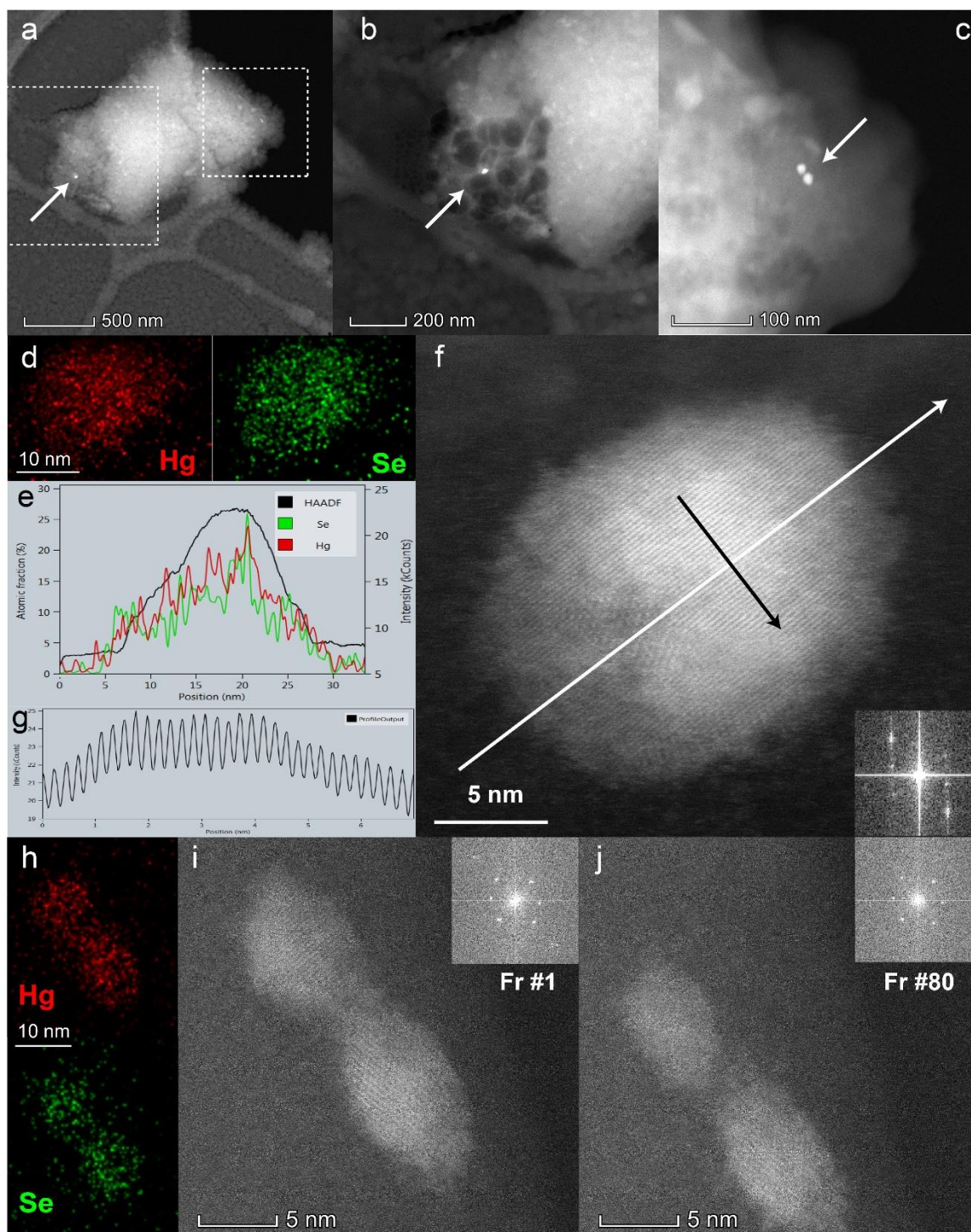
Figure S12. Small aggregates of ~30 nm HgSe$_{NP}$ and isolated 5 to 20 nm HgSe$_{NP}$ were imaged in the pectoral muscles of petrel P4, owing to the high scattering power of Hg and Se embedded in a thick and beam-sensitive organic matrix. a) STEM-HAADF image at -170°C of a dried piece of muscle. b) HAADF image of the region pointed out with an arrow in (a) after degradation of the organic matrix under the electron beam. The HgSe grain was not altered under the beam, as confirmed by the HR-STEM contrast in (f). c) Magnification of the right framed area in (a) revealing two HgSe$_{NP}$ (same as those shown in Fig. 5c). d) EDX maps of Hg (red) and Se (green) from the HgSe$_{NP}$ pointed out in (c). e) Post-

S24

acquisition EDX line profile (position and direction shown in (f)) of the atomic fraction of Hg (red) and Se (green), and HAADF contrast profile (black, in kcounts), confirming the HgSe composition of the nanoparticle. f) HR-STEM-HAADF image (5 µs per 17 pm pixel) of the 15 x 20 nm HgSe$_{NP}$ pointed out in (b). The FFT in inset indicates that the Hg-Se grain has a HgSe cubic structure. g) Intensity periodic profile along the black arrow (100 pixel wide) of image (f). h) EDX maps of Hg (red) and Se (green) of the two HgSe$_{NP}$ pointed out in (c). i-j) First (i) and 80th (j) HR-STEM-HAADF images (acquired after the 7 min long EDX maps), with corresponding FFT patterns, of the two HgSe$_{NP}$. The twinned nanoparticles drifted under the 60 pA electron beam, but their crystal structure was preserved. The image shown in Figure 5c is the sum of the 24 first frames of the time series after correction of the drift artifact. To prevent damaging the HgSe$_{NP}$ and minimize their displacement during the degradation of the organic matrix, the total electron dose was drastically reduced by diminishing the counting time per pixel. The conditions of the acquisitions were 0.2 µs per 12 pm pixel size (instead of 20 µs for other HAADF images), for a total of 0.1 sec per frame and a cumulated dose of 4733 e-/A^2.
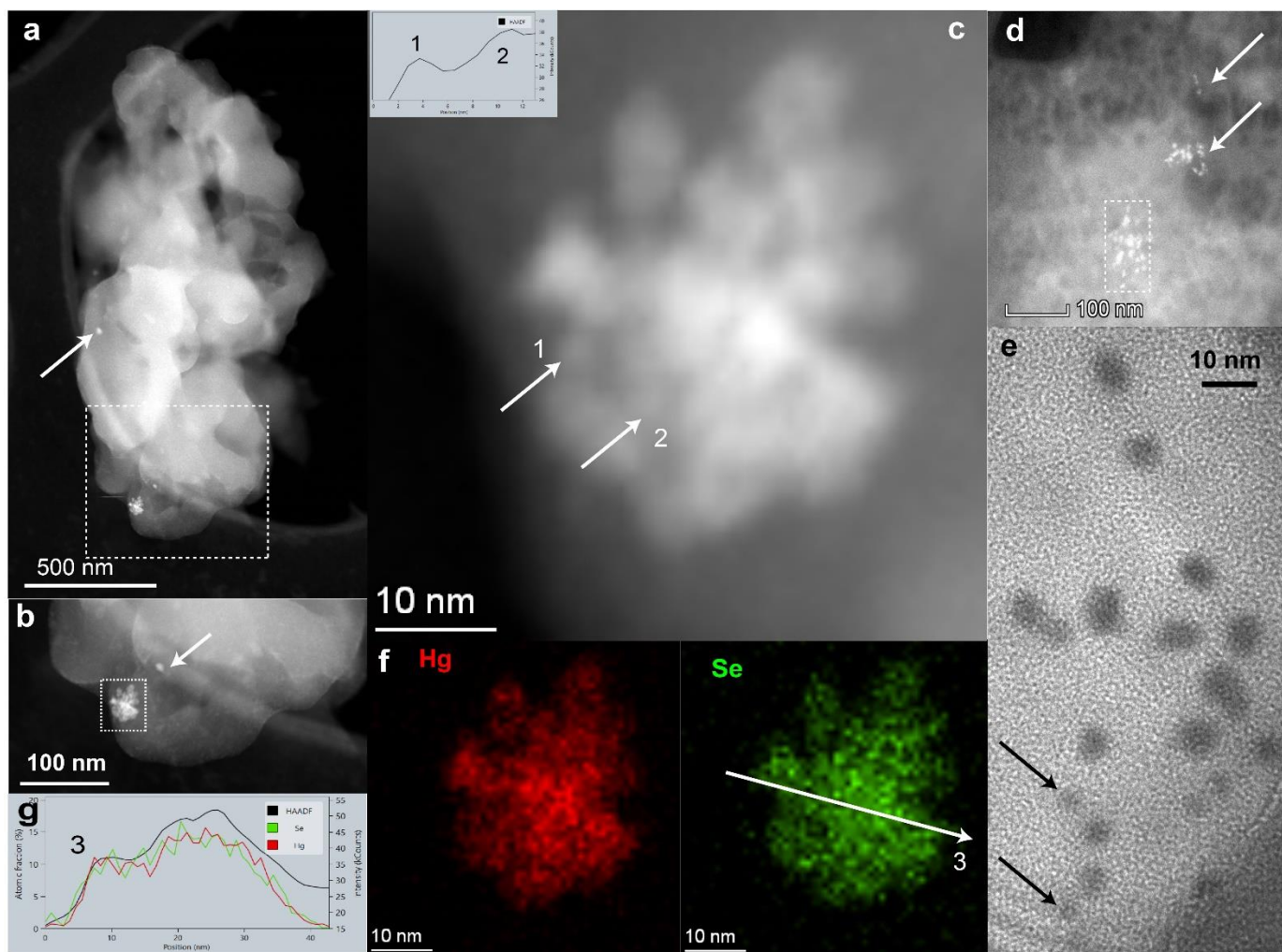
Figure S13. a) STEM-HAADF image of a piece of dried pectoral muscle of petrel P4. b) zoom of the framed area in (a). Arrows in (a) and (b) point out small HgSe_NP aggregates. c) STEM-HAADF image of the large HgSe aggregate framed in (b). Arrows 1 and 2 point out two nanograins. Their size is about 2 nm, as indicated by the HAADF intensity profile shown in inset. d) STEM-HAADF image of isolated HgSe_NP in another region of the sample. e) TEM image of the HgSe_NP grains located in the squared area of d). Black arrows point out NP of ~4 nm. f) EDX maps of Hg (red) and Se (green) of the aggregate in (c). The white arrow indicates the position and direction of the EDX line profile 3 in (f). g) Post-acquisition EDX line profile 3 of Hg (red) and Se (green) in atomic fraction (%), with the HAADF contrast (black – in kcounts), showing that the HgSe_NP are stoichiometric.
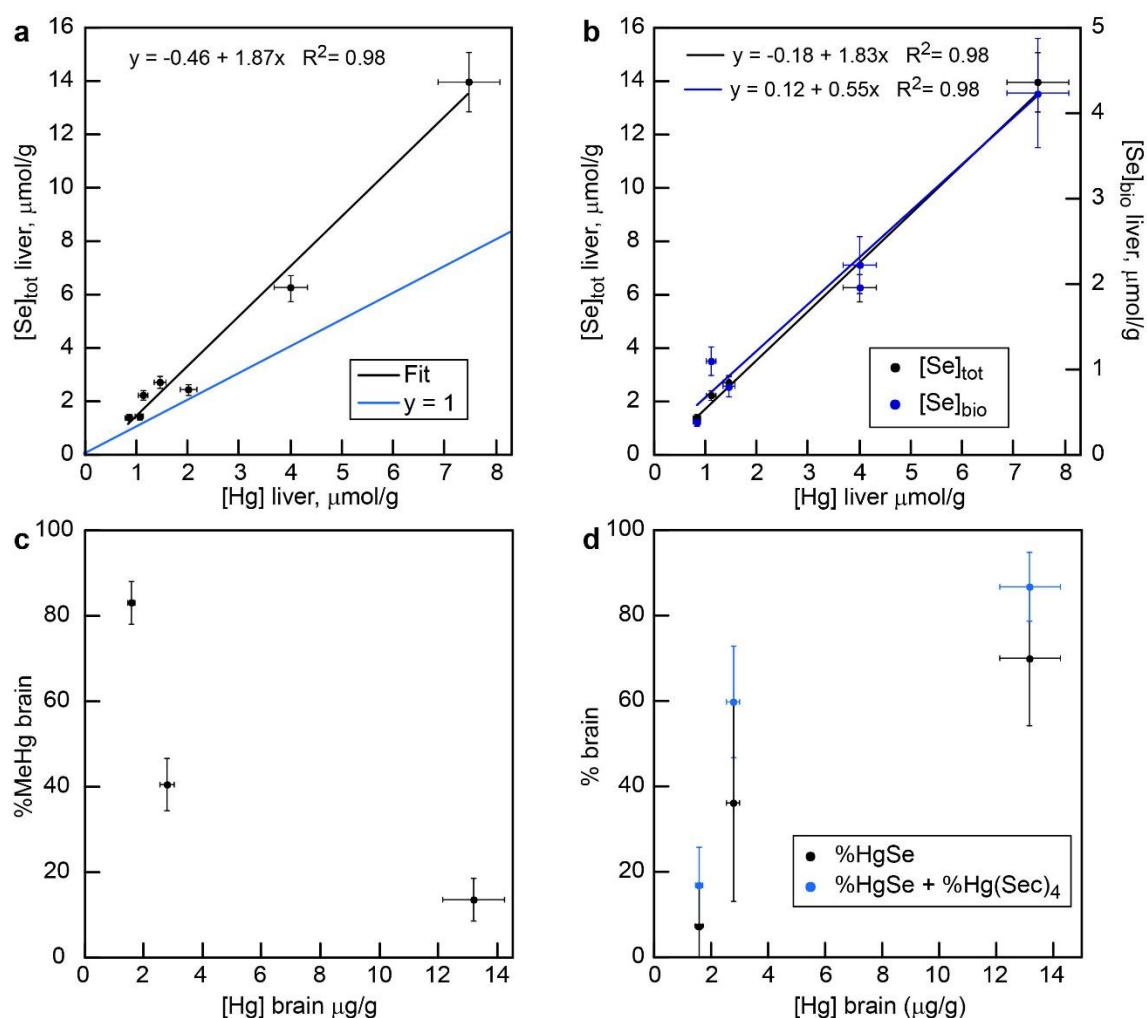
Figure S14. a) Total concentration of Se against total concentration of Hg in the liver of giant petrels P1-P6 and P8 with straight line corresponding to the 1:1 ratio. b) Total and bioavailable concentrations of Se against total concentration of Hg in the liver of individuals P1-P5. c) Molar proportion of methylmercury against total Hg concentration in the brain of individuals P6-P8. d) Molar proportions of HgSe and HgSe+Hg(Sec)$_4$ against total Hg concentration in the brain of individuals P6-P8.
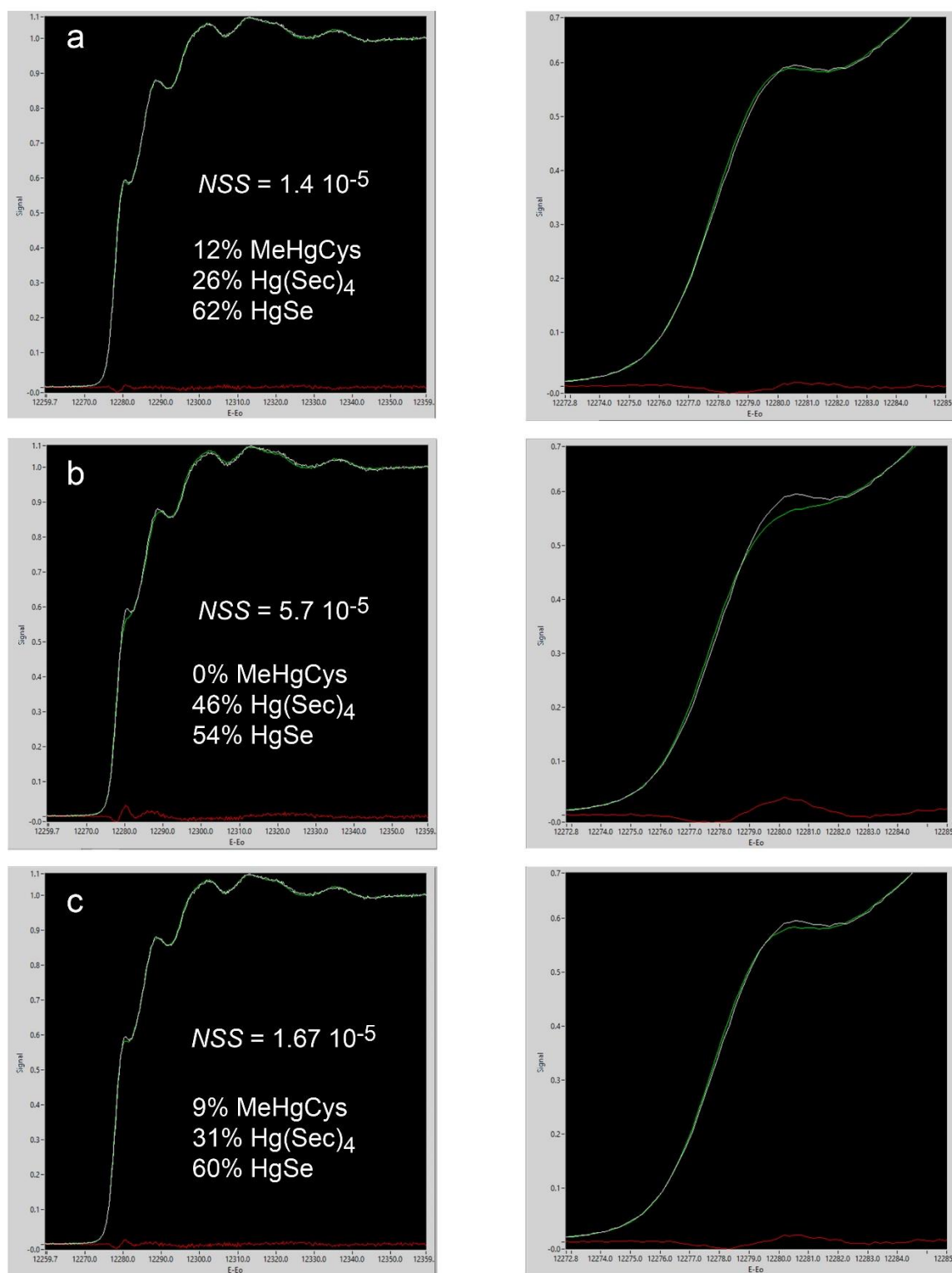
Figure S15. Sensitivity of HR-XANES to MeHgCys mixed with HgSe and Hg(Sec)$_4$ illustrated with the kidneys spectrum of petrel P3. a) Best-fit calculation with the three Hg species (Table S2). The optimal molar percentage of MeHgCys is 12%. b) Best-fit calculation without MeHgCys. c) Best-fit calculation with the percentage of MeHgCys fixed to 9% instead of 12%. The fit residual has increased by 20% relative to the best-fit value, and the calculated near-edge peak clearly lacks intensity. The spectra on the right column are an enlargement of the near-edge region.

S7. Supplementary references

(1) Carravieri, A.; Bustamante, P.; Churlaud, C.; Cherel, Y. Penguins as bioindicators of mercury contamination in the Southern Ocean: Birds from the Kerguelen Islands as a case study. *Sci. Tot. Environ.* **2013,** *454*, 141-148.

(2) Rovezzi, M.; Lapras, C.; Manceau, A.; Glatzel, P.; Verbeni, R. High energy-resolution x-ray spectroscopy at ultra-high dilution with spherically bent crystal analyzers of 0.5 m radius. *Rev. Sci. Instr.* **2017,** *88*, 013108.

(3) Cattell, R. B. The scree test for the number of factors. *J. Multiv. Behav. Res.* **1996,** *1*, 245–276.

(4) Malinowski, E. R. Determination of the number of factors and the experimental error in a data matrix. *Anal. Chem.* **1977,** *49*, 612-617.

(5) Malinowski, E. R. *Factor Analysis in Chemistry*. John Wiley and Sons, New York: 2002.

(6) Malinowski, E. R. Statistical F-tests for abstract factor analysis and target testing. *J. Chemom.* **1988,** *3*, 49-60.

(7) Malinowski, E. R. Statistical F-tests for abstract factor analysis and target testing: Erratum. *J. Chemom.* **1990,** *4*, 102.

(8) Malinowski, E. R. Theory of error for target factor-analysis with applications to mass-spectrometry and nuclear magnetic-resonance spectrometry. *Anal. Chim. Acta-Comp.* **1978,** *2*, 339-354.

(9) Manceau, A.; Marcus, M. A.; Tamura, N. Quantitative speciation of heavy metals in soils and sediments by synchrotron X-ray techniques. In *Applications of Synchrotron Radiation in Low-Temperature Geochemistry and Environmental Science*, Fenter, P. A.; Rivers, M. L.; Sturchio, N. C.; Sutton, S. R., EDX. Mineralogical Society of America: Washington, DC, 2002; Vol. 49, pp 341-428.

(10) Marcus, M. A.; MacDowell, A. A.; Celestre, R.; Manceau, A.; Miller, T.; Padmore, H. A.; Sublett, R. E. Beamline 10.3.2 at ALS: a hard X-ray microprobe for environmental and materials sciences. *J. Synchrotron Radiat.* **2004,** *11*, 239-247.

(11) Isaure, M. P.; Laboudigue, A.; Manceau, A.; Sarret, G.; Tiffreau, C.; Trocellier, P.; Hazemann, J. L.; Chateigner, D. Quantitative Zn speciation in a contaminated dredged sediment by μPIXE, μSXRF, EXAFS spectroscopy and principal component analysis. *Geochim. Cosmochim. Acta* **2002,** *66*, 1549-1567.

(12) Kim, C. S.; Bloom, N. S.; Rytuba, J. J.; Brown, G. E. Mercury speciation by X-ray absorption fine structure spectroscopy and sequential chemical extractions: A comparison of speciation methods. *Environ. Sci. Technol.* **2003,** *37*, 5102-5108.

(13) Senn, A. C.; Kaegi, R.; Hug, S. J.; Hering, J. G.; Mangold, S.; Voegelin, A. Composition and structure of Fe(III)-precipitates formed by Fe(II) oxidation in water at near-neutral pH: Interdependent effects of phosphate, silicate and Ca. *Geochim. Cosmochim. Acta* **2015,** *162*, 220-246.

(14) Voegelin, A.; Pfenninger, N.; Petrikis, J.; Majzlan, J.; Plotze, M.; Senn, A. C.; Mangold, S.; Steininger, R.; Gottlicher, J. Thallium speciation and extractability in a thallium- and arsenic-rich soil developed from mineralized carbonate rock. *Environ. Sci. Technol.* **2015,** *49*, 5390-5398.

(15) Manceau, A.; Wang, J.; Rovezzi, M.; Glatzel, P.; Feng, X. Biogenesis of mercury-sulfur nanoparticles in plant leaves from atmospheric gaseous mercury. *Environ. Sci. Technol.* **2018,** *52*, 3935–3948.

(16) Ressler, T. WinXAS: a program for X-ray absorption spectroscopy data analysis under MS-Windows. *J. Synchrotron Radiat.* **1998,** *5*, 118-122.

(17) Ankudinov, A. L.; Rehr, J. J. Relativistic calculations of spin-dependent X-ray-absorption spectra. *Phys. Rev. B* **1997,** *56*, 1712-1716.

(18) Rodic, D.; Spasojevic, V.; Bajorek, A.; Onnerud, P. Similarity of structure properties of $Hg_{1-x}Mn_xS$ and $Cd_{1-x}Mn_xS$ (structure properties of HgMnS and CdMnS). *J. Mag. Mag. Mater.* **1996,** *152*, 159-164.

(19) Earley, J. W. Description and synthesis of the selenide minerals. *Am. Miner.* **1950,** *35*, 337-364.

(20) Manceau, A.; Marcus, M.; Lenoir, T. Estimating the number of pure chemical components in a mixture by X-ray absorption spectroscopy. *J. Synchrotron Radiat.* **2014,** *21*, 1140-1147.

(21) Manceau, A. In preparation. **2020**.

(22) Moscoso-Londono, O.; Carriao, M. S.; Cosio-Castaneda, C.; Bilovol, V.; Sanchez, R. M.; Lede, E. J.; Socolovsky, L. M.; Martinez-Garcia, R. One-step room temperature synthesis of very small γ-Fe_2O_3 nanoparticles. *Mater. Res. Bull.* **2013,** *48*, 3474-3478.